Distribution Agreement

In presenting this thesis as a partial fulfillment of the requirements for a degree from Emory University, I hereby grant to Emory University and its agents the non-exclusive license to archive, make accessible, and display my thesis in whole or in part in all forms of media, now or hereafter now, including display on the World Wide Web. I understand that I may select some access restrictions as part of the online submission of this thesis. I retain all ownership rights to the copyright of the thesis. I also retain the right to use in future works (such as articles or books) all or part of this thesis.

Joseph Ara Ambarian March 23, 2023

Crystallographic Characterization of Novel Glucose and Lactate Biosensors

by

Joseph Ara Ambarian

Dr. Katherine Davis
Adviser

Chemistry

Dr. Katherine Davis

Adviser

Dr. Christine Dunham

Committee Member

Dr. Fang Liu

Committee Member

2023

Crystallographic Characterization of Novel Glucose and Lactate Biosensors

By

Joseph Ara Ambarian

Dr. Katherine Davis

Adviser

An abstract of
a thesis submitted to the Faculty of Emory College of Arts and Sciences
of Emory University in partial fulfillment
of the requirements of the degree of
Bachelor of Science with Honors

Chemistry

2023

Abstract

Crystallographic Characterization of Novel Glucose and Lactate Biosensors
By Joseph Ara Ambarian

Glucose metabolic pathways are potential therapeutic targets for epilepsy, Alzheimer's disease, Huntington's disease, and other neurological disorders. An intimate understanding of cerebral energy metabolism opens doors for the development of novel treatments, and obtaining this understanding requires advanced imaging techniques that intimately capture the activities of glucose and other energy metabolites in the mammalian brain. The Yellen Lab at Harvard Medical School designed two genetically encoded fluorescence lifetime-based biosensors, SweetieTS and LiLac, which allow for *in vivo* tracking of glucose and lactate, respectively. Upon ligand binding, each biosensor undergoes a conformation change that results in an observable change in fluorescence lifetime. Mutagenesis studies conducted in the Yellen lab offer insights into the mechanism of coupling and lifetime change in these biosensors; however, they also raise questions that require additional structural information to answer. Here, we used X-ray crystallography to solve the structures of SweetieTS and LiLac and corroborate our collaborators' hypotheses. The two sub-2.5 Å crystal structures presented suggest that a linker between the two domains in each biosensor regulates solvent exchange near the chromophore. Ligand binding causes the linker to shift. This changes the amount of solvent quenching, which determines the lifetime of the biosensor. Though additional crystal structures of the biosensors in different states would be helpful in understanding these processes in more detail, this work continues an important conversation about the mechanism of lifetime change in these genetically encoded biosensors. Fluorescence lifetime imaging has been limited by the lack of efficient strategies to design lifetime biosensors: These insights will advance the development of new genetically encoded biosensors for fluorescence lifetime imaging.

Crystallographic Characterization of Novel Glucose and Lactate Biosensors

By

Joseph Ara Ambarian

Dr. Katherine Davis

Adviser

A thesis submitted to the Faculty of Emory College of Arts and Sciences
of Emory University in partial fulfillment
of the requirements of the degree of
Bachelor of Science with Honors

Chemistry

2023

Acknowledgements

I would like to thank my committee members, Dr. Christine Dunham and Dr. Fang Liu, and my research advisor Dr. Katherine Davis for her consistent support and mentorship. I would also like to thank our collaborators at Harvard Medical School, especially Paul Casciola Rosen, Dr. Dorothy Koveal, and Dr. Gary Yellen. The collaborative efforts, guidance, and encouragement of my graduate mentor Sam Horwitz and lab-mate Lidia Waidmann have been crucial to the success of this project and my development as a chemist. Thank you to Ruth Nelson, Sam Lee, Steve Gaunt, Israel Negrete-Abreu, and Schuyler Arn, and my parents and siblings for your constant support.

Table of Contents

Table of Figures

INTRODUCTION

Mapping Energy Metabolism in the Brain

ATP is the currency of biological energy and an allosteric modulator.[1] In the brain, 95% of the ATP supply is produced by glucose metabolism.[2] As such, regional shifts in glucose metabolism can change the accessibility of ATP, thereby activating or deactivating cellular processes.[3] A method of hijacking glucose metabolism and controlling the flow of ATP could offer potential treatments for neurological diseases by slowing pathogenic processes that rely on particular ATP concentrations.[3, 4]

This is an active area of epilepsy research.[3] Epilepsy is characterized by neuronal hyperexcitability, manifesting as recurring seizures.[5] Presumably, glycolysis is localized near the cell membrane in neuronal cytosol, which in turn localizes glycolytic ATP near K_{ATP} pumps in the membrane.[6] ATP inhibits K_{ATP} pumps, which raises neuronal excitability.[7] Reducing glycolytic ATP concentrations may lower neuronal excitability and potentially reduce the likelihood of seizures.[3] Other studies suggest that upregulation of the pentose phosphate pathway,[8] heightened levels of ketosis,[9] and other energy-metabolic processes are also anticonvulsant. Deeper understanding of these processes could inform the development of potential therapeutics for epilepsy.[3]

Moreover, glucose metabolism is dysregulated in neurodegenerative diseases, including Alzheimer's disease, Parkinson's disease, Huntington's disease, and frontotemporal dementia, and may accelerate disease progression and worsen symptoms. Methods of restoring healthy energy supply to the brain is of interest in developing novel treatments.[4]

Pioneering these hypothetical treatments for the aforementioned diseases requires a deep understanding of the specificities of cerebral glucose metabolism. Acquiring this

understanding requires improved tools with high spatial and temporal resolution that can map glucose metabolism in animal models and brain slices, where biology is most similar to natural metabolism in humans.[3, 10] *In vitro* studies, and even single-cell studies, deviate significantly from natural human biology; i*n vivo* and *ex vivo* studies, especially in mammalian models, are more relevant to human disease.[10] For the purposes of this paper, the disputed terms *in vivo* and *ex vivo* refer specifically to *in live animal models* and *in brain slices*, respectively.

Autoradiography and positron emission tomography have been historically useful methods of mapping glucose in the human brain.[10, 11] However, their spatial resolution is on the order of 10 µm and 100 µm, respectively, while subcellular resolution is on the order of 0.1 µm (100 nm).[12-14] The temporal resolution of these methods is also low, posing additional challenges for quantitation.[10] Fluorescence microscopy (FM) offers high temporal resolution and spatial resolution on the order of 10-100 nm, on par with the sizes of subcellular compartments (**Figure 1**).[14] Developments in two-photon microscopy techniques have improved the compatibility of FM *in vivo* and *ex vivo*.[15] The longer wavelengths utilized in two-photon FM allow deep penetration into tissue (0.5-1.0 mm).[14] Using FM to map cerebral glucose metabolism in live-animal models or brain slices requires an intracellular fluorescent indicator that undergoes a fluorescence change in the presence of glucose or another relevant metabolite. This change can be detected, providing information about the presence—and with more advanced techniques, the quantity—of a metabolite. Fluorescence microscopy has undergone iterative changes in recent decades, becoming progressively more effective at mapping metabolic processes *in vivo* and *ex vivo*.[16]

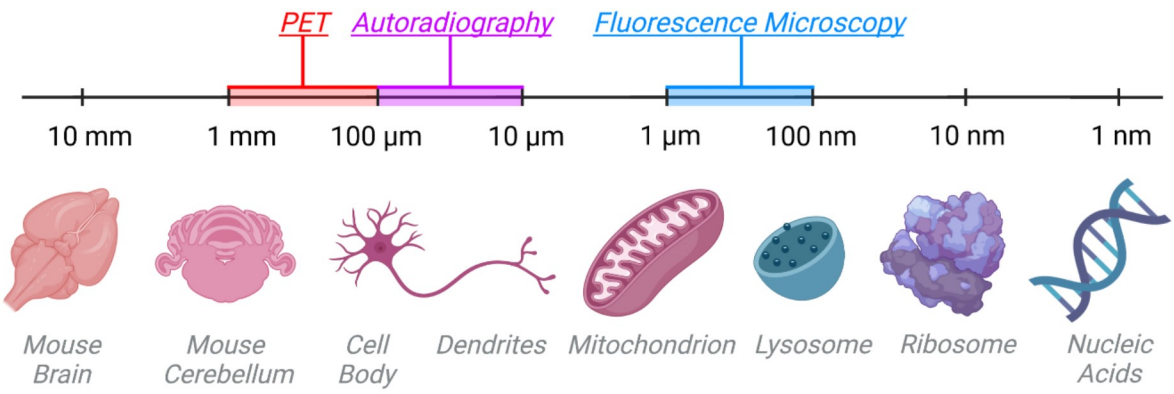

Figure 1. Resolution of neurological imaging techniques. Fluorescence microscopy offers high enough spatial resolution to distinguish signals within subcellular compartments. Biological structures of decreasing size are also displayed on the scale, listed by the order of magnitude of their approximate size. [14, 17-20] Created with BioRender.com; adapted from Carter et al.[14]

Genetically Encoded Fluorescent Indicators

As mentioned, fluorescence microscopy *in/ex vivo* requires a fluorescent indicator that interacts with a metabolite of interest from *within* a living model. There are two strategies used to place fluorescent indicators in a living animal. The first, delivery of exogenous chemical probes into the host, offers high quantum yield but can involve challenges with biocompatibility, delivery, and spatial control in an *in/ex vivo* context.[21] Genetically encoded fluorescent indicators (GEFIs; adapted from *GEIs*[22]) overcome these challenges and are an increasingly popular alternative.[21, 23] GEFIs offer the ability to probe specific cell types[10, 23] and subcellular compartments,[24] while also being compatible with longitudinal studies *in vivo*.[25] FM paired with GEFIs offer a powerful technique for tracking glucose and relevant metabolites *in vivo* and *ex vivo*.

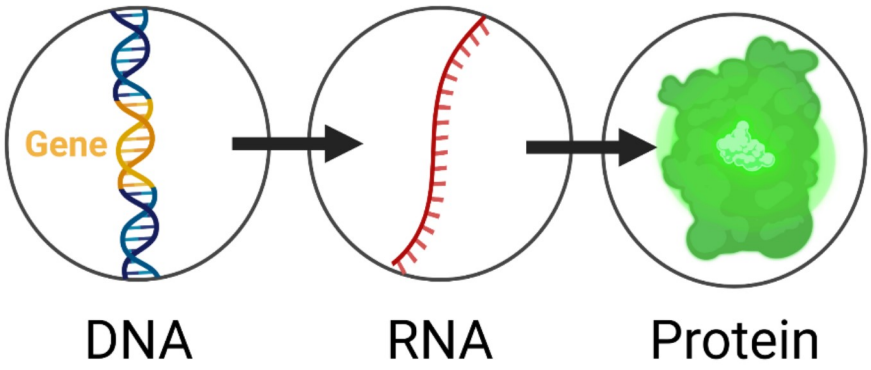

Figure 2. Genetically encoded fluorescent indicators. A gene (yellow) encoding a protein-based fluorescent indicator is introduced into a genome. Following the central dogma, the gene is transcribed into mRNA (red), then translated, producing an active protein-based indicator (green). Created with BioRender.com.

Like exogenous fluorescent probes, GEFIs are molecules whose fluorescent properties change upon interaction with a target metabolite in the cell. As the name implies, a gene encoding the GEFI is incorporated into the genome of the host. The sequence is then transcribed and translated into a fully functioning protein-based indicator in the cell (**Figure 2**).

Numerous design strategies have been employed, but GEFIs typically consist of a *sensing* domain and a *reporting* domain.[22] The former undergoes a chemical or mechanical change in the presence of a target analyte. This change is transferred to the reporting domain via a *coupling* mechanism. Coupling is the extent that analyte binding in the sensing domain causes a fluorescence change in the reporting domain. Linkers between the sensing domain and reporting domain are often responsible for transferring this mechanical change from the former to the latter.[22]

Sensing domains are typically derived from a microbial ligand binding domain. High-specificity periplasmic binding proteins are often used as sensors because they evade biological

cross-talk.[26] The reporting domain is a fluorescent protein, typically a derivative of green fluorescent protein from *Aequorea victoria* (avGFP).[22, 27] avGFP has since been engineered for enhanced and distinctive spectral characteristics, resulting in a large, diverse family of mutant FPs.[28] GFP, and all of its variants, are characterized by an 11-stranded β-barrel enclosing a chromophore.[29] The avGFP chromophore is a cross-link of *S65-Y66-G67* (SYG) residues, which are first translated as individual amino acids. Upon folding, functionality lining the interior of the β barrel elicits formation of the chromophore.[30] A hydrogen bonding networks secures this chromophore in a rigid position (**Figure 3**), preventing non-radiative decay via rotation; capping strands on either end of the barrel protect the local environment of the chromophore from rapid solvent exchange, which also quenches fluorescence.[31, 32]

The sensing domain, reporting domain, and their linker must be engineered to ensure that the GEFI can respond to metabolite concentration changes within a physiological range. This *sensing range* should be optimized to align closely with the physiologically relevant range of ligand concentration;[22] if designed appropriately, GEFIs are an invaluable tool for *in vivo* imaging of energy metabolism.

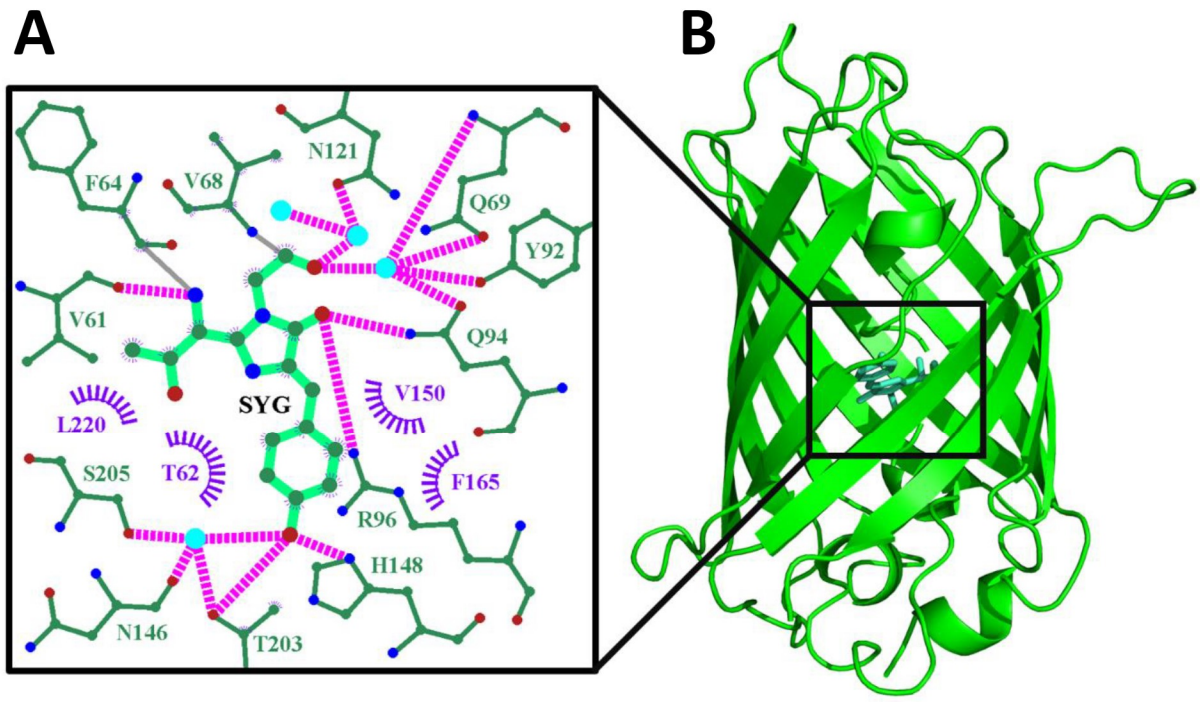

Figure 3. The green fluorescent protein. **(A)** The signature chromophore of GFPs, SYG, is shown in emerald green. Residues within 3.5 Å (forest green) of the chromophore engage in hydrogen bonding (fuchsia). Residues engaging in hydrophobic interactions with the chromophore are shown in purple. Created with LIGPLOT.[33] **(B)** The chromophore is supported by a central α helix, running through the β barrel, as shown in the crystal structure reported by Ormo et al.[32] Generated in PyMOL Molecular Graphics System.

Practical Challenges & Solutions

GEFIs can be used for high resolution, tunable microscopic studies of energy metabolism *in vivo* and *ex vivo*. However, each GEFI has limitations that are specific to the design of the indicator and its corresponding readout. These limitations qualify the conclusions that can be drawn from them. In recent decades, successive generations of sensors have been developed to overcome these limitations.[16]

The GEFIs most commonly used to map glucose metabolism are fluorescence intensity-based indicators; analyte binding causes either an increase or decrease in the GEFI's fluorescence

output. In an intensity-based indicator, the sensing domain undergoes a confirmation change upon analyte binding, which causes a change in the immediate environment of the reporting domain's chromophore.[22, 24] However, the signal cannot be interpreted as directly translatable to a quantifiable analyte concentration.[16] Large concentrations of GEFIs surrounded by little analyte can give the same output as fewer GEFIs surrounded by highly concentrated analyte. GEFI concentrations must be accounted for, but calibration in a cell is challenging because it requires permeabilizing the cell; in doing so, you risk diluting sensor concentration.[15] Relative comparisons between cells are also challenging because signal differences could be attributed to differing expression levels in each cell rather than analyte concentration.[10, 15, 16]

Ratiometric intensity-based indicators overcome many of these challenges by rendering fluorophore concentrations irrelevant. If a single GEFI gives out two different signals, the ratio of their signal will (1) be dependent on analyte concentration and (2) remain independent of fluorophore concentrations.[15, 16] An "emission-ratiometric" indicator gives off two fluorescent signals with distinct wavelengths. The ratios of these two signals will change in the presence of different analyte concentrations. Intramolecular FRET sensors are an example.[34] Two FPs are coupled to the sensor domain, and their emission intensities will differ in the presence of varying analyte concentrations.[15, 16] Having two FP domains on the same indicator introduces complexity: Distinct FPs will have distinct photostability and maturation rates, and each FP will involve different wavelength dependent scattering in tissue. Responsibly using these GEFIs *in vivo* or *ex vivo* requires complex calibration and data interpretation, complicated further across samples and experiments.[15]

Excitation-ratiometric intensity-based indicators will absorb two wavelengths at ratios that are dependent on analyte concentration. These GEFIs typically involve a sensor domain bound to one, circularly permuted FP, overcoming the challenges of having two FPs. Circular permutation brings the linkers closer to the chromophore such that ligand binding changes the chromophore's local environment.[16, 22] Changes in its immediate hydrogen bonding network will alter its pKa. The anionic and neutral chromophore absorb at different wavelengths, so absorbance wavelength depends on analyte concentration. These sensors still face challenges of wavelength dependent scattering in tissue, with the additional caveat of high pH sensitivity.[16, 22]

Ratiometric or not, intensity-based indicators pose several obstacles for calibration, quantitation, and data interpretation in tissue.[15] Fluorescence lifetime-based indicators offer an alternative. The readout for lifetime GEFIs is not a change in fluorescence intensity, but rather fluorescence lifetime—the amount of time the fluorophore stays in its excited state after excitation.[16] FPs are coupled to a ligand-sensing domain such that ligand binding causes a change in the chromophore's lifetime by changing the accessible mechanisms of quenching: Quenching lowers lifetime.[31] The chromophore's rotational freedom and access to solvent or other quenchers determine the GEFI's readout, so ligand binding must impact one of these processes.[10, 15]

Lifetime GEFIs are not dependent on concentration. If the signal is strong enough to be detected, concentrations can be identified. Photobleaching is not a concern, as lifetime will not change with diminishing intensity.[15] These biosensors offer significant advantages, and they are invaluable in many biological contexts, but specifically for *in vivo* studies in the brain.

Fluorescence-Lifetime Imaging: LiLac & SweetieTS

Our collaborators in the Yellen Group at Harvard Medical School designed the first lifetime-based GEFI for lactate—an energy metabolite—as well as the first for glucose. Both lifetime GEFIs were kindly named in accordance with their respective ligands: *SweetieTS* binds glucose, and *LiLac* binds lactate (**Figure 4**). Both have been successfully used for *ex vivo* studies to give quantitative concentrations of their respective ligands.[10, 35] The SweetieTS sensing domain is a periplasmic glucose binding protein from *Thermus thermophilus*[36] coupled at its hinge region to a circularly permuted T-Sapphire,[37] a mutant GFP. The protein was designed by replacing the circularly permuted EGFP domain of an intensity-based glucose indicator with a T-Sapphire, followed by coupling optimization.[38] LiLac, the lifetime-based lactate GEFI was built via the *Beadscan* screening system.[35] Its sensing domain is the chemoreceptor TlpC from *Helicobacter pylori*,[39] which is coupled to a split mTurquoise, a mutant cyan FP.[40]

Our collaborators sought to elucidate each sensor's coupling mechanism—the structural behavior that causes binding in one domain to change the fluorescence of another. They performed mutagenesis studies on both SweetieTS and LiLac, the results of which are unpublished at this time. Tentative conclusions were drawn regarding the coupling mechanisms at work in each GEFI: (1) Analyte binding to the sensing domain determines the positioning of the linker, which is involved in opening or closing a "hole" in the β barrel. [41] This gap would allow solvent to rapidly exchange near the chromophore, quenching fluorescence[31] and lowering lifetime in response to changes in the sensing domain. Also, (2) specific residues neighboring the linker play a role in positioning this linker.

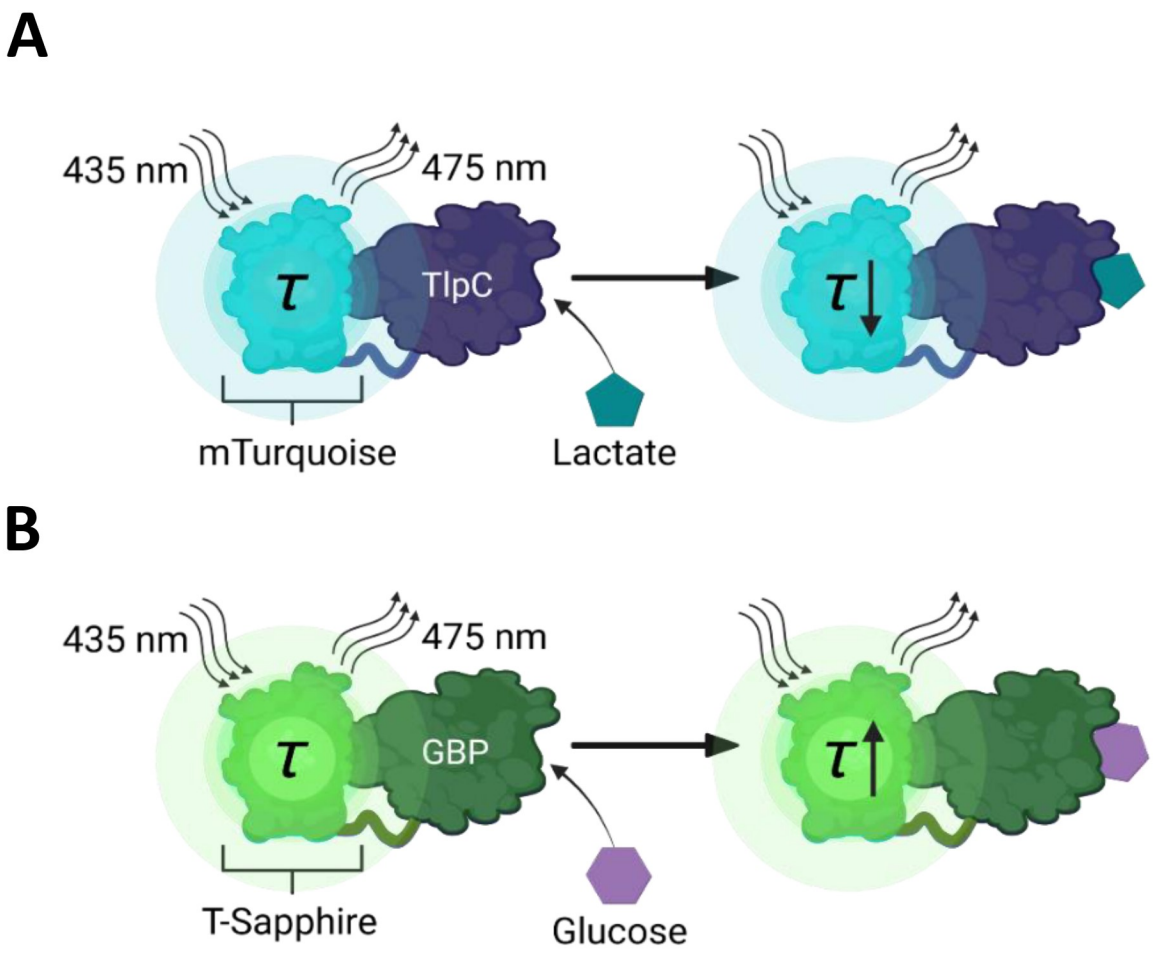

Figure 4. Lilac & SweetieTS. **(A)** Upon lactate binding, LiLac's lifetime drops from 3.4 ns to 2.2 ns. **(B)** Conversely, upon glucose binding, SweetieTS's lifetime increases from 1.6 ns to 1.95 ns. Created with Biorender.com.

AIM I

Our collaborators conducted these mutagenesis studies to gain a mechanistic understanding of how coupling and lifetime-change work in these two lifetime GEFIs. The absence of mechanistic understanding has slowed development of fluorescence lifetime indicators, as there is not a well-established rationale to be followed when attempting to design these probes.[35]

Though helpful in developing this mechanistic understanding, mutagenesis studies on LiLac and SweetieTS leave gaps to be filled. We aim to learn specifics about how linkers are involved in sealing the β barrel and how residues neighboring the linker also play a role. We proposed using X-ray crystallography to elucidate the structure of these two GEFIs, clarifying and complimenting conclusions drawn from our collaborators' mutagenesis studies. This process involves crystallizing and solving the respective crystal structures of LiLac and SweetieTS in both their bound and unbound states. Therefore, their high and low lifetime states can be compared, especially in relation to ligand binding.

These structural insights could inform rational modifications of the SweetieTS and LiLac design to improve their coupling, leading to more advanced probes in the study of cerebral glucose metabolism. More broadly, structural understanding of how this fluorescence-lifetime coupling occurs could serve as a blueprint toward the design of other lifetime-based indicators. More stream-lined development of these advanced GEFIs would be a monumental stride in our ability to study health-relevant processes *in vivo* and *ex vivo*.

METHODS I

Protein Crystallization

The typical workflow of protein X-ray crystallography consists of (1) crystallizing the protein, (2) irradiating crystals with intense X-rays to observe diffraction, and (3) structure solution, refinement, and validation (**Figure 5**). The process began upon receiving purified SweetieTS and LiLac, stored in buffer (25 mM MOPS, 90 mM KCl, 10 mM NaCl, pH 7.4), from the Yellen Lab.

The first step, protein crystallization, involves several rounds of screening to determine appropriate conditions that facilitate crystal growth. In all screens, 1-2 µL of protein-containing crystallization buffer is added to 1 equivalent of a second "reservoir" solution, forming a drop. Reservoir solutions contain some combination of salt to stabilize charges on the protein, crowding agent to push protein into a supersaturated state that facilitates crystallization, and buffer to maintain an appropriate pH for crystallization.[42]

Crystallizing protein requires first identifying an optimal protein concentration—overly diluted protein will not interact with itself as required for crystallization, and overly concentrated protein will precipitate out of solution. The Hampton Pre-Crystallization Test™ was used to determine appropriate protein concentrations. Protein drops are prepared in 2 to 4 experimentally determined buffers. Formation of "light precipitate" correlates to the lowest likelihood of clear drops and precipitation in a broad screen. This method conserves protein, as an ideal protein concentration can be identified without expending high amounts of protein to conduct a full screen.[43]

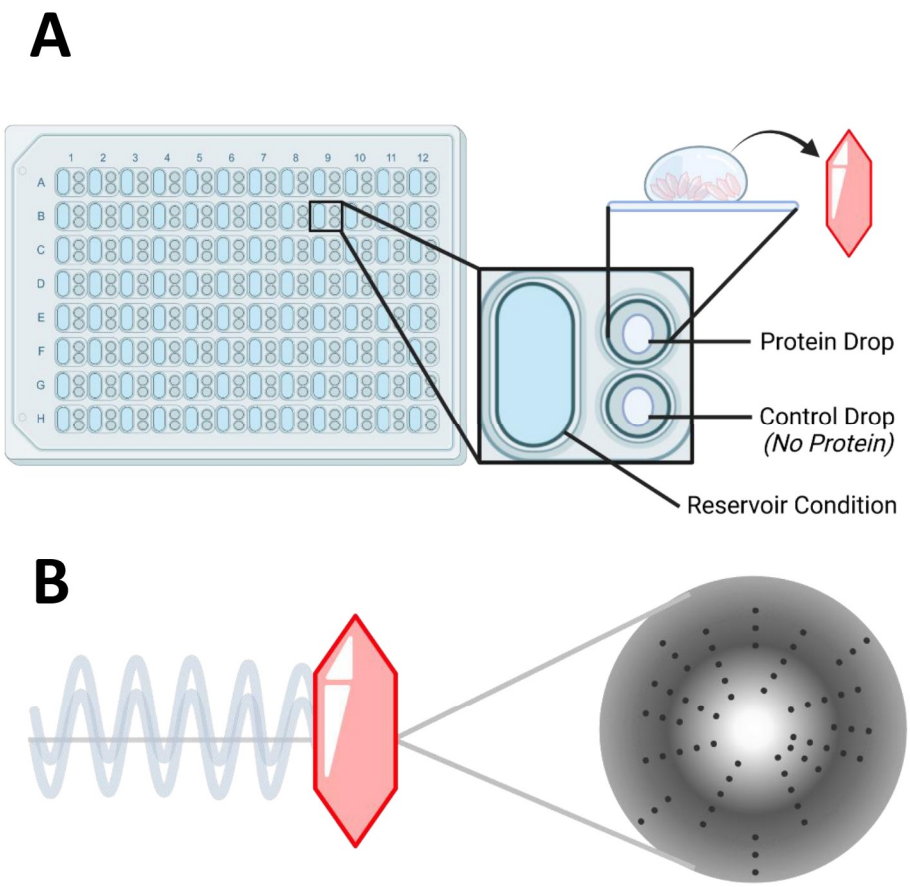

Figure 5. Protein X-ray crystallography. **(A)** 96 well plates are prepared with reservoir, protein drops, and control drops as labeled. **(B)** After crystals grow, they are shipped in cryogenic conditions to a synchrotron, where they are irradiated with intense X-rays and the resulting diffraction patterns are collected. Created with Biorender.com.

Once an appropriate protein concentration is determined, sparse matrix screens are prepared. 96 distinct reservoir solutions supplied by Hampton Research are added to each reservoir well in the 96 well plate. 1-2 µL of each reservoir is added to 1 equivalent of the protein-containing buffer, as previously described. Screens are checked immediately and then intermittently after the date of preparation. When hits are identified—defined as translucent, birefringent entities in a drop—the reservoir condition can be optimized via a secondary screen. Secondary screens consist of varying the concentrations of the components of an initial hit

(**Figure 6**). The optimization process repeats from optimization to optimization until crystals that diffract are produced.

Slight modifications are made to the above procedures to obtain a crystal structure of a protein bound to a ligand, such as glucose or lactate. Proteins can be *co-crystallized* with a ligand by introducing high concentrations of that ligand into the crystallization buffer; ideally, any crystals that form contain the protein in a ligand-bound state. Alternatively, the protein could be crystallized without adding ligand first. These crystals could then be *soaked* in a buffer containing high concentrations of ligand, allowing the ligand to penetrate the crystal lattice and bind with the protein *in crystallo*.[44]

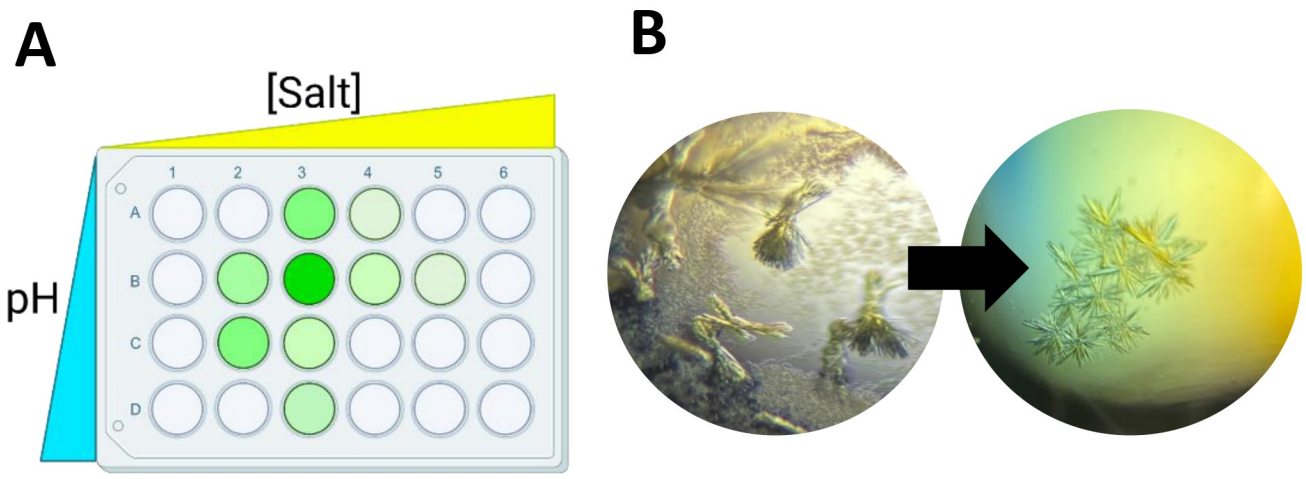

Figure 6. Optimizing crystallization conditions. **(A)** Secondary screens are conducted in 24 well plates, varying some parameter across one axis (ie. pH, [salt], etc.), and another across the second. If a particular set of conditions produces more, larger, or more geometric hits, as indicated by the opaquer greens, then that condition should be optimized. In the illustration shown, B3 would be ideal for optimization in another screen. **(B)** SweetieTS was optimized to produce better morphology crystals, which diffracted. Better geometry is typically an indicator of "diffractability," though not necessarily. Created with Biorender.com.

Protein X-ray Crystallography

Single protein crystals greater than 25 µm were placed into a cryoprotectant containing up to 30% of either glycerol or ethylene glycol. Crystals were then stored in cryogenic conditions to protect crystal morphology and shipped to Argonne National Laboratory for data collection. All diffraction data were collected with an Eiger X 16M detector at beamline 23-ID-B of the Advanced Photon Source. Data were collected sequentially with an incident wavelength of 1.033 Å and Δϕ of 0.2° for all crystals, which were maintained at 100K. The data were indexed, integrated, and scaled in S4XDS and merged in AIMLESS.[45, 46] Chimeric molecular replacement was done in PHASER,[47] with component domains of each sensor. Model building was done in Coot,[48] and refinement was done in Phenix.[49]

RESULTS I

LiLac

Although LiLac crystals were iteratively optimized, the only crystals to appreciably diffract (**Figure 7B**) formed in the original sparse matrix screen after 4 months (**Table 1**). The structure was solved via molecular replacement using a chimeric search model, composed of mTurquoise2 (PDB: 6YLN; 100% sequence identity)[40] and HpTlpC (PDB: 5WBF; 100% sequence identity). [39]

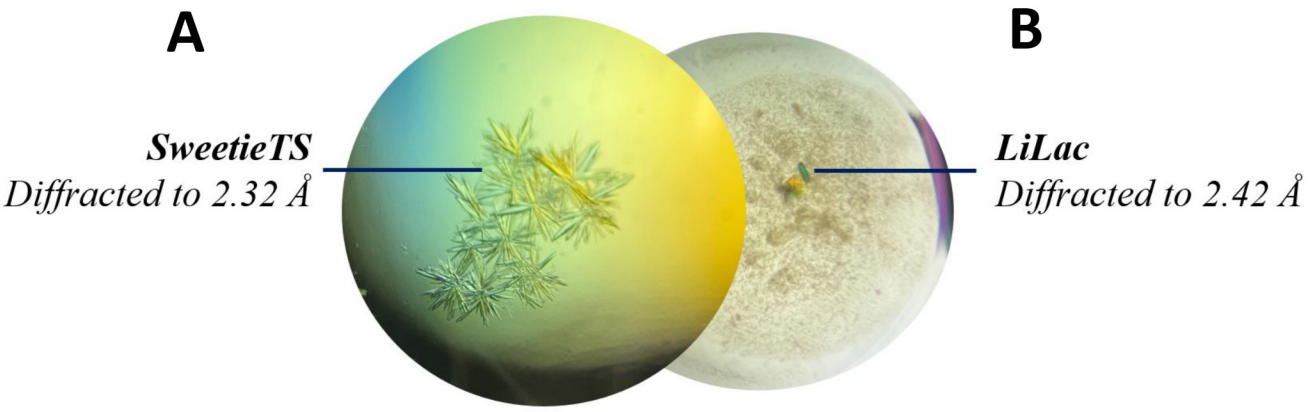

Figure 7. Crystals that appreciably diffracted.

Table 1. Conditions producing crystals that appreciably diffracted**.** Asterisks (*) indicate crystals from which data was processed for molecular replacement.

		Buffer System	pH	[Crowding Agent]	[Salt]	[Other]	[Protein]	[Ligand]	Resolution
Lilac	*	0.1M HEPES	7.5	25% PEG 3350	0.2M $MgCl_2 \bullet 6H_2O$	—	6.75 mg/mL	—	2.42Å
SweetieTS	*	0.1M Tris	8.5	25% PEG 3350, 3% MEG	0.2M NH_4OAc	—	5.5 mg/mL	5·[Protein]	2.32Å
	*	0.1M Tris	8.5	25% PEG 3350	0.2M NH_4OAc	—	3.5 mg/mL	—	2.15Å
		0.1M Tris	8.5	25% PEG 3350	0.2M NH_4OAc	10 mM Urea	5.5 mg/mL	—	~2.79Å
		0.1M Tris	8.5	25% PEG 3350	0.2M NH_4OAc	2 mM L-Glutathione	5.5 mg/mL	—	~3.30Å

Refinement and model building were conducted until R-values plateaued. Data collection and refinement statistics are shown in **Table 2**. The LiLac crystals did not form in a condition containing lactate, suggesting that the sensor was unbound *in crystallo*. There was electron density in the binding pocket, but it is difficult to distinguish lactate from solvent. A polder map was generated in Phenix, but it failed to distinguish the density from bulk solvent with certainty.

To determine if lactate was bound, the TlpC domain of LiLac was overlayed with the HpTlpC/lactate complex (PDB: 5WBF) published by Machuca et al.[39] The LiLac binding domain shows significant deviation from the published lactate-bound HpTlpC in the lactate binding site. A loop composed of Y369-T378 is flipped out of the binding pocket in LiLac, but the analogous loop in the published, bound HpTlpC is flipped inward toward lactate (**Figure 8**). The root mean square deviation (RMSD) for the entirety of the LiLac TlpC domain and the published HpTlpC domain is 2.387 Å, which drastically jumps to 3.235 Å when comparing the specific region containing this loop, E363 to F388. It is important to note that the LiLac structure is pending validation via clash score, Ramachandran, rotamer, and geometric analysis, and while broad conclusions about the main-chain can be drawn with confidence, side-chain positions and RMSD values are tentative.

In the published TlpC structure, the positioning of this loop allows the backbone amides of L252 and S253 to hydrogen bond with lactate. In LiLac, the analogous residues, L372 and S373, are over 10 Å away from lactate's binding site. To my knowledge, no data is available to indicate whether lactate can bind without forming these hydrogen bonding interactions. Also, to my knowledge, there is no published structure of an unbound TlpC domain to compare with the Lilac structure. We can tentatively conclude that lactate is not bound.

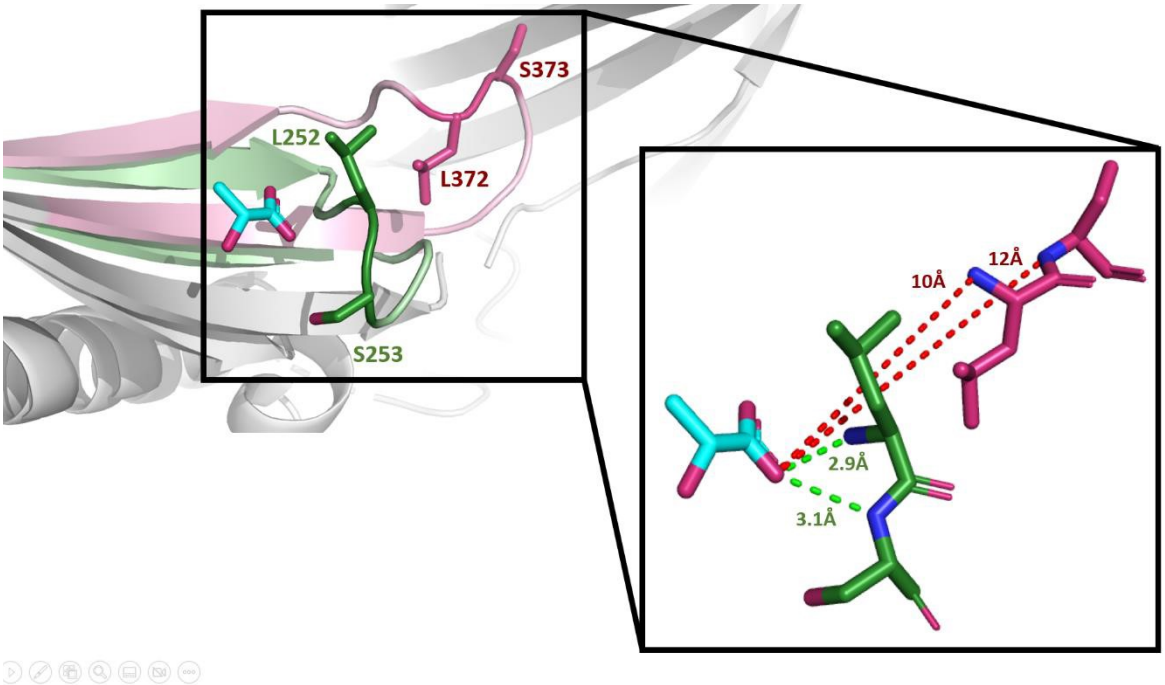

Figure 8. LiLac binding residue alignment. The Y369-T378 loop in Lilac (pink) deviates drastically from the analogous loop on the published HpTlpC/lactate complex (green). The binding residues L372 and S373 are shifted too far to be H-bonding. This corroborates the conclusion drawn from the limited density in the binding pocket. Generated in PyMOL.

Considering the LiLac structure (**Figure 10A**) to be unbound, immediate next steps consisted of trying to crystallize the LiLac/lactate complex. Three strategies were taken to crystallize this complex. Unbound LiLac crystals from the condition that successfully diffracted were soaked with lactate. Secondly, LiLac was crystallized in the condition that produced unbound, diffracting LiLac crystals, but with excess lactate. Thirdly, a sparse matrix screen was prepared with excess lactate in the crystallization buffer. None of the strategies yielded LiLac crystals that diffracted appreciably; only the unbound LiLac crystal structure was obtained.

SweetieTS

SweetieTS formed crystals that appreciably diffracted in several conditions: All were optimization screens, shown in **Table 1**. The two data sets that were processed are indicated with

asterisks in **Table 1**. A search model was constructed from a *S65G*,*Y66S*-GFP (PDB 2G5Z; 97.5% identity)[50] and the *T. thermophilus* Glucose Binding Protein (TtGBP) (PDB 2B3F; 98.5% identity)[36] for chimeric molecular replacement. Refinement and model building were conducted until R-values plateaued. Statistics are shown in **Table 2**.

One of the SweetieTS crystals from which data was collected and processed was grown in a condition containing glucose, while the second crystal was not (**Table 1**). This suggests that both a bound and an unbound structure were obtained. However, upon model building and refinement, the crystal structures were identical, both containing density in the binding pocket. A polder map was generated, and it signified the presence of a ligand in the binding pocket of both structures.

However, after modelling-in glucose, there were no hydrogen bonding interactions between glucose and the SweetieTS binding pocket residues. Overlaying the GBP domain of SweetieTS with the glucose-bound TtGBP (PDB: 2B3B)[36] published by Cuneo et al. resulted in a tentative (*SweetieTS structure is pending validation*) RMSD of 3.353 Å. In SweetieTS, a loop consisting of residues E32-T62 had fallen out of the binding pocket, whereas in the published, bound GBP, this loop was tucked into the binding pocket. The only residue on this loop involved in binding is T39, which was mutated to A39 in SweetieTS to weaken binding in the GEFI. With no binding interactions requiring this E32-T62 loop to be located near the glucose, the structure of SweetieTS could reasonably deviate from the TtGBP/glucose structure while still being bound to glucose. Deleting the E32-E62 loops in both SweetieTS and TtGBP/glucose dropped the RMSD down to 2.459 Å. With significant density in the binding pocket and a structure comparable to the published TtGBP/glucose complex, we believe that SweetieTS is bound and in a high-lifetime

state in both structures. These structures will be complete (**Figure 10B**), pending more appropriate fitting of glucose, as well as validation, via clash score, Ramachandran, rotamer, and geometric analysis. However, one of the solved SweetieTS structures presents a deviation from expectation, in that SweetieTS bound glucose without glucose being added to the crystallization condition. One possible explanation is that glucose, present in *E. coli* cells during expression, remained bound through purification.

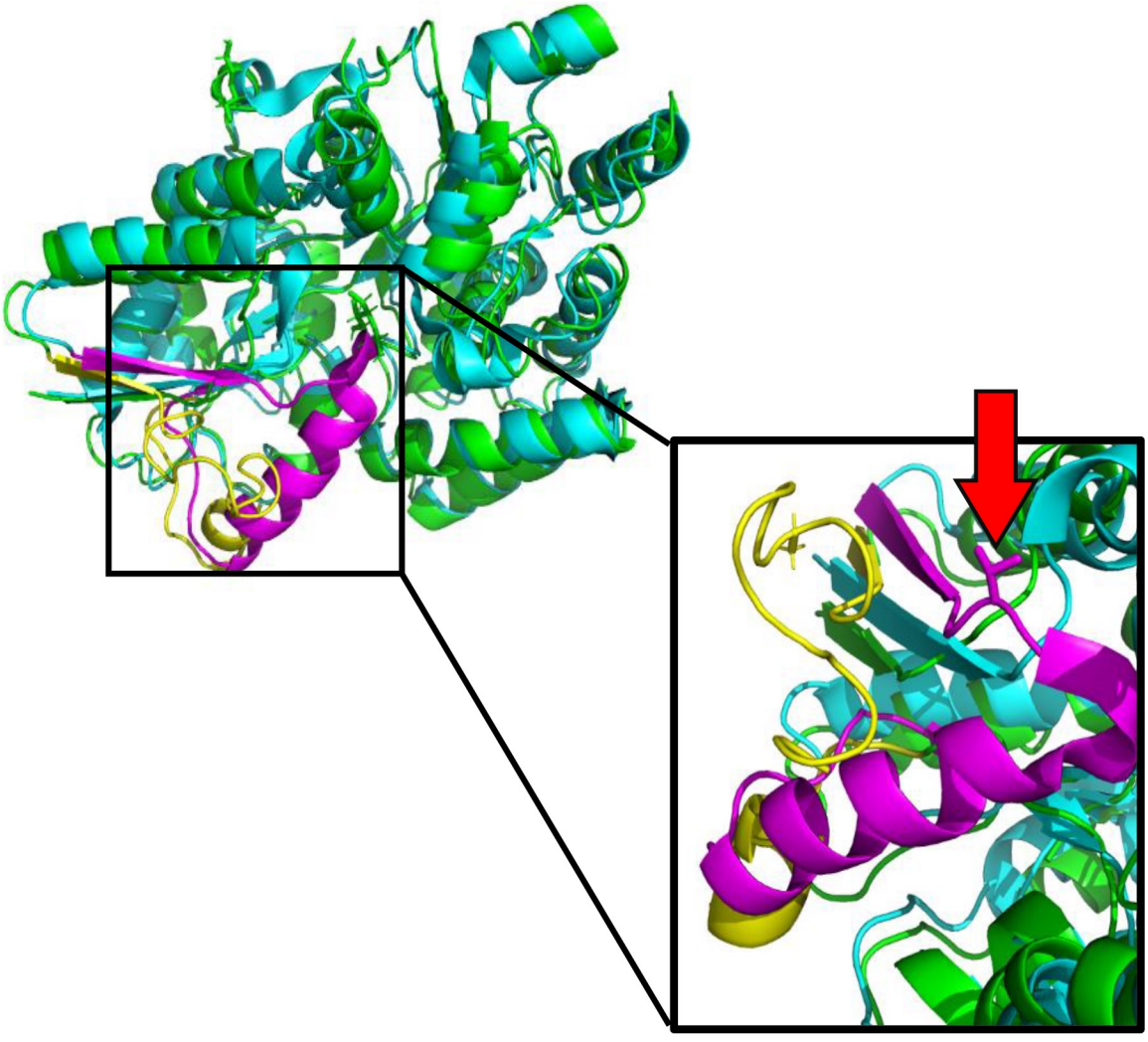

Figure 9. Sweetie overlayed with TtGBP. SweetieTS's TtGBP domain (green) deviates slightly from the reported bound structure of TtGBP (cyan). The largest deviation occurs on the loop containing residues E32-T62. SweetieTS is shown in yellow, and the reported TtGBP is shown in magenta. The red arrow points toward a threonine in the reported TtGBP, facing inwards toward glucose. This residue is mutated to alanine in SweetieTS. Generated in PyMOL.

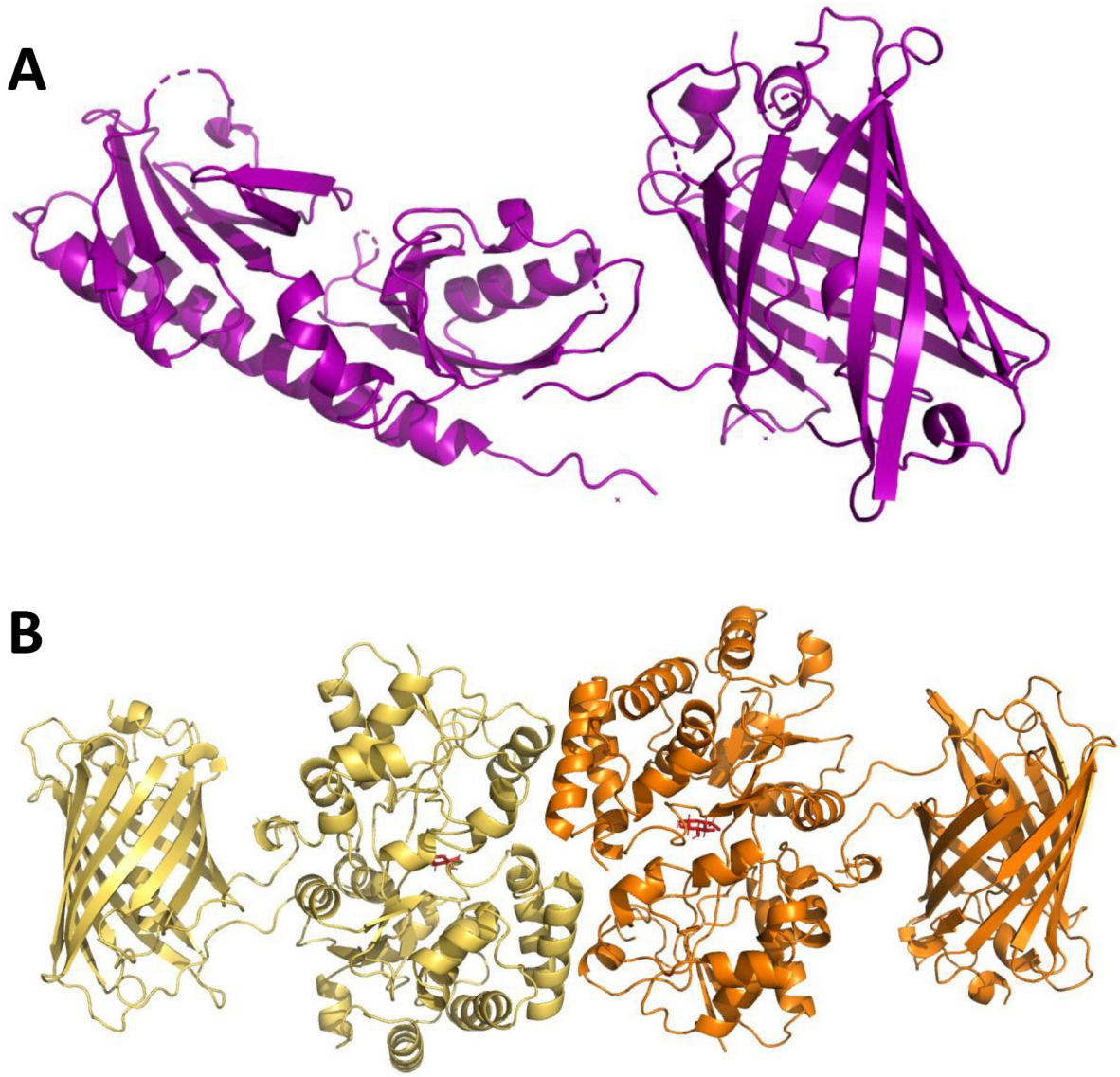

Figure 10. Crystal structures of LiLac and SweetieTS. Both structures are pending validation. **(A)** One LiLac molecule occupies a unit cell, whereas **(B)** two SweetieTS molecules occupy a unit cell. Glucose is shown in red. Generated in PyMOL.

Table 2. Data collection & refinement statistics for LiLac and SweetieTS. Values for the higher resolution shell are indicated in parentheses.

	LiLac	SweetieTS
Resolution range (Å)	46.13 - 2.42 (2.507 - 2.42)	47.9 - 2.32 (2.403 - 2.32)
Space group	P 1	P 1 2_1 1
Unit cell (Å) (degrees)	34.35 57.98 67.319 97.819 91.427 104.238	97.691 63.716 117.363 90 93.711 90
Total reflections	31881 (3451)	217324 (22386)
Unique reflections	16456 (1775)	62078 (6206)
Multiplicity	1.9 (2.0)	3.5 (3.6)
Completeness (%)	86.92 (92.11)	98.72 (99.49)
I/σ_1	13.06 (1.88)	11.23 (1.59)
Wilson B-factor	63.87	51.06
R-merge	0.03066 (0.3756)	0.06259 (0.6451)
R-meas	0.04336 (0.5312)	0.07405 (0.7599)
R-pim	0.03066 (0.3756)	0.03913 (0.3974)
CC 1/2	0.999 (0.865)	0.998 (0.792)
CC*	1 (0.963)	0.999 (0.94)
Reflections (Refinement)	16518 (1764)	62026 (6199)
Reflections (R-free)	1637 (174)	1996 (197)
R-work	0.2515 (0.3728)	0.2112 (0.2990)
R-free	0.2886 (0.4143)	0.2495 (0.3768)
CC (work)	0.944 (0.796)	0.957 (0.834)
CC (free)	0.938 (0.557)	0.962 (0.699)
No. of non-hydrogen atoms	3477	9830
Macromolecules	3452	9549
Ligands	37	126
Solvent	2	199
Protein residues	463	1244
RMS (bonds) (Å)	0.033	0.009
RMS (angles) (degrees)	1.65	1.01
Ramachandran favored (%)	85.62	96.67
Ramachandran allowed (%)	10.34	2.27
Ramachandran outliers (%)	4.04	1.06
Rotamer outliers (%)	18.99	2.58
Clashscore	26.9	7.03
Average B-factor	79.1	55.44
Macromolecules	79.18	55.63
Ligands	64.96	42.74
Solvent	96.87	51.96

AIM II

With mixed success in our first round of experiments, we obtained an unbound LiLac structure and a glucose-bound SweetieTS structure—both show the GEFIs in their high-lifetime state. This makes sense: High-lifetime GEFIs have sealed β barrels—well-ordered proteins are more compatible with crystallization.[51] However, for a holistic understanding of the coupling mechanisms of each GEFI, we need structures of both the bound and unbound states. No crystals of unbound SweetieTS nor bound LiLac successfully diffracted, even after several rounds of screening.

SweetieTS crystals showed glucose-binding, even when glucose was not added to the crystallization drop. As such, our collaborators were able to send us the plasmids of two SweetieTS variants with lower binding affinity: SweetieTS-K66H and SweetieTS-L276V. The next aim involved crystallizing these two proteins for X-ray crystallography to obtain an unbound SweetieTS structure. Moreover, solving the structures of the K66H and L276V variants would be especially rewarding, as our collaborators found that these mutants have improved coupling and a *higher* high-lifetime state. GEFIs with a larger gap between their high-readout and low-readout states can have broader sensing ranges.[22]

LiLac did not bind to lactate after several rounds of screening with excess lactate concentrations. Unfortunately, no LiLac mutant has higher binding affinity than the original. Instead, our collaborators sent us LiLac-F423A. This mutant is locked in a low lifetime state, with poor coupling (*lactate binding shifts the lifetime from 2.5 ns to 2.25 ns*). Ideally, a crystal structure of this mutant LiLac can provide additional information about factors that kill coupling. With this,

we began tackling our second set of aims—to solve crystal structures of mutant SweetieTS and mutant LiLac as a means of overcoming the challenge of crystallizing their low-lifetime states.

METHODS II

SweetieTS Mutants: Expression

The Yellen Group at Harvard Medical School expressed and purified LiLac-F423A and provided stocks of the mutant LiLac sensor for us to begin crystallization. Our collaborators also provided pRSetB plasmids for the two SweetieTS mutants with lower binding affinities, SweetieTS-K66H and SweetieTS-L276V. K66H and L276V variants were expressed in house. The plasmid map for SweetieTS is shown in **Figure 11**. The K66H and L276V plasmids deviate from this plasmid by one codon. Both K66H and L276V plasmids contained the genes encoding the GEFI, a polyhistidine (His)-tag, and neomycin/kanamycin resistance. The His-tag was included to allow the purification of the sensors via a Ni^{2+} affinity column, and antibiotic resistance is included to ensure that only bacteria transformed with the plasmid would grow in the kanamycin-supplemented broth during expression.

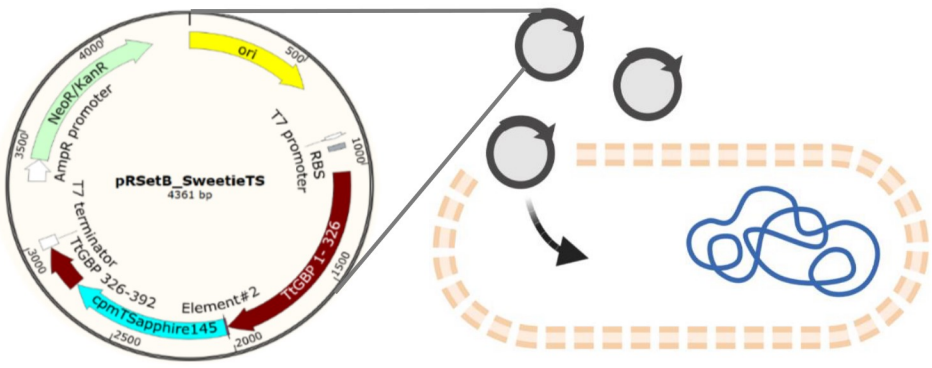

Figure 11. Transformation of the pRSetB_SweetieTS plasmid. Transformation was done via heat shock. Created with Biorender.com.

K66H and L276V plasmids were suspended in 50µL of deionized water and incubated at room temperature for 15 minutes. 2 µL of diluted plasmid was added to BL21(DE3) cells, which were transformed with their respective plasmid via heat shock at 42°C for 30 seconds. Cells were placed on ice, and 500 µL of super optimal broth with catabolite repression was added. Transformed cells were incubated at 37°C for 1 hour, before plating each on LB Agar plates supplemented with 50 µg/mL kanamycin.

After ~48 hours of growth at room temperature, single colonies were isolated and used to inoculate 1L cultures of Terrific Broth supplemented with kanamycin (50 µg/mL). Cultures grew at 37°C, shaken at 200 rpm for 16 hours, to an OD600 nm of ~3.0, in accordance with an optimized protocol provided by the Yellen Group. Cultures were cooled on ice for ~20 minutes and allowed to equilibrate to room temperature for ~45 minutes before induction (1 mM IPTG). Cultures were then incubated at 18°C, 220 rpm for ~18-24 hours.

SweetieTS Mutants: Lysis & Purification

The BL21 cells were harvested via centrifugation at 4°C, 9000 g, for 15 minutes. Lysis buffer (50 mM NaH_2PO_4, 300 mM NaCl, and 10 mM imidazole, pH 8.0) was supplemented with chicken egg white lysozyme (0.1 mg/mL) and 1 tab complete EDTA-free protease inhibitor per 25 mL buffer. To solubilize tabs before adding BL21 pellets, the buffer was incubated at 10°C for 180 rpm for 30 minutes in 250 mL Erlenmeyer flasks. Cell pellets were then resuspended in lysis buffer, at 5 mL/g of buffer. Cells were lysed via sonication for 15 minutes on ice (30% power, 45 seconds on/15 seconds off). Cell lysates were left on ice for ~15 minutes, before spinning down at 4°C, 20000 rpm, for 20 minutes.

At this point, the purifications of L276V and K66H were split between myself and colleague, Lidia Waidmann; I purified K66H, which is reported below.

The supernatant for the K66H expression was flowed over a Ni^{2+} affinity, gravity column (15 mL/column volume), which was then washed with 10 column volumes (CVs) of lysis buffer. The affinity column was next washed with 10 CVs of another wash buffer (50 mM NaH_2PO_4, 300 mM NaCl, 20 mM imidazole, pH 8.0), followed by 3 CVs of elution buffer (50 mM NaH_2PO_4, 300 mM NaCl, 500 mM imidazole, pH 8.0) (**Figure 12A**).

SDS-PAGE gel electrophoresis was used to analyze samples taken from the flow-through, buffer washes, and eluate of the Ni^{2+} affinity chromatography (**Figure 12B**). SDS-PAGE gel shows further purification was needed after the affinity column, which dictated our decision to further purify via size exclusion chromatography (SEC).

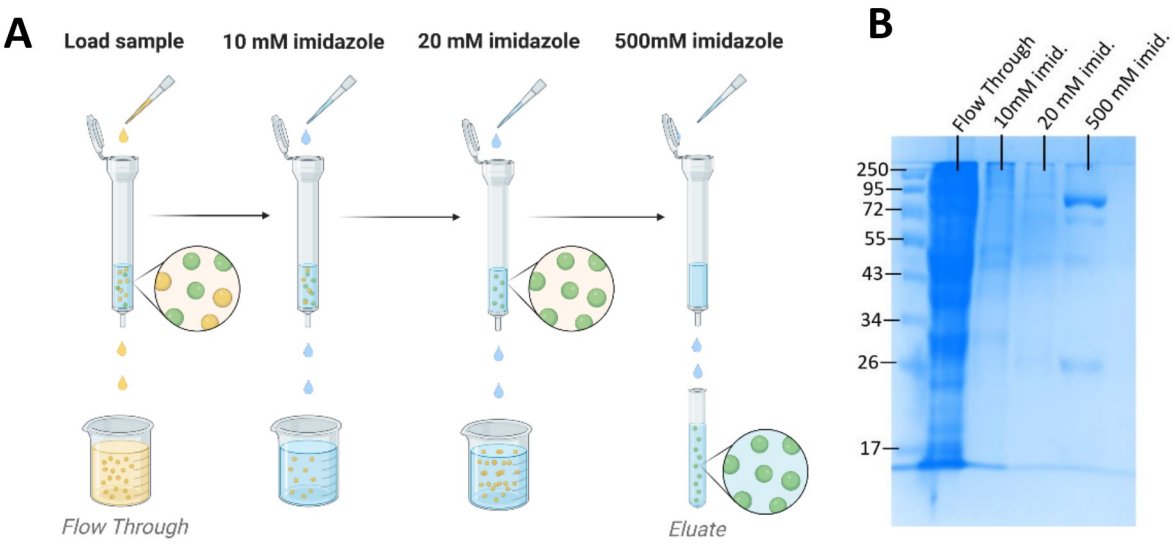

Figure 12. Ni^{2+} affinity chromatography. **(A)** The scheme shows sample loading, the 2 wash steps, and the elution, in accordance with an optimized procedure provided by our collaborators. **(B)** The gel shows our 75.1 kDa protein eluting as expected. It also shows impurities near the 26 kDa mark. Created with Biorender.com.

The eluate containing crude K66H was concentrated down to 2.5 mL, using 30-kDa spin filters at 4°C, 4000 rpm, for 30 min. K66H was loaded onto a PD-10 desalting column and exchanged into an SEC running buffer (150 mM NaCl, 2 mM dithiothreitol, 2 mM MgCl2, 5% CHAPS, 50 mM NaHEPES, pH 7.4). SEC was conducted on a Fast Protein Liquid Chromatograph (FPLC). K66H eluted as a monomer at approximately 0.55 column volumes, or 66 mL, as indicated by aromatic amino acid absorbance at 280 nm and the SYG chromophore absorbance at 399 nm (**Figure 13**). Fractions 62-72 were combined for K66H, and each protein sample was concentrated down to 2.5 mL, then exchanged into a buffer for crystallization (25 mM MOPS, 90 mM KCl, 10 mM NaCl, pH 7.4). Measurements on the nanodrop indicate that the yield was approximately 1 mL of 800 mg/mL K66H, which was sufficient to begin screening.

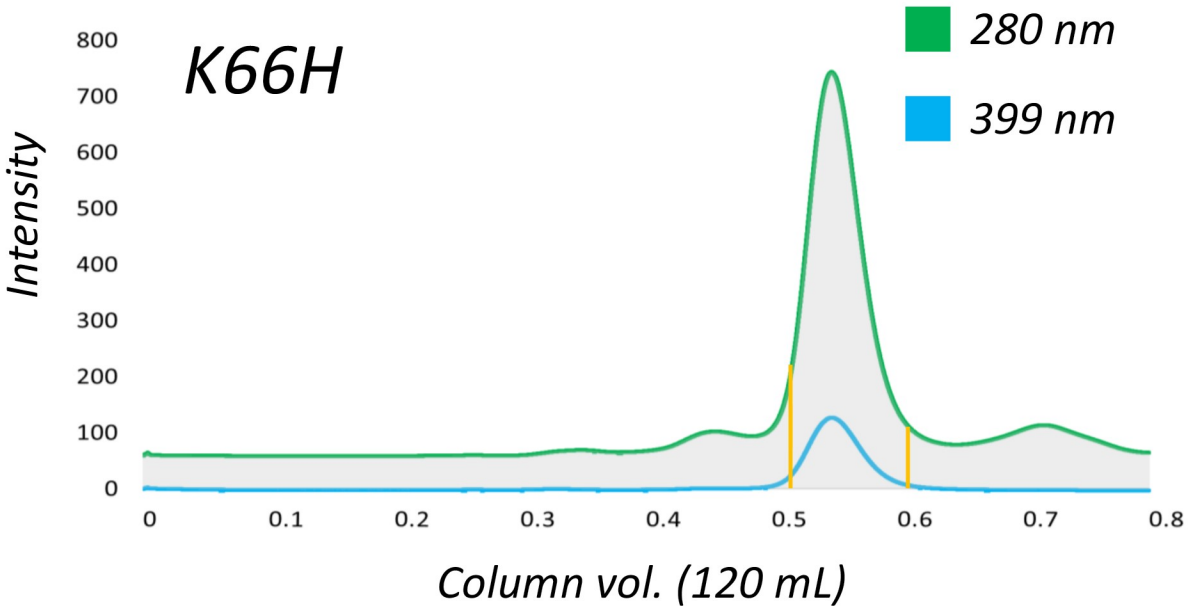

Figure 13. Size exclusion chromatograph for SweetieTS-K66H. Yellow lines indicate the fractions that were collected.

Protein X-ray Crystallography

SweetieTS-L276V, SweetieTS-K66H, and LiLac-F423A were then screened for an ideal crystallization condition. For an in-depth methodology describing protein crystallization, see *Methods I*.

Upon crystallization, SweetieTS-L276V, SweetieTS-K66H, and LiLac-F423A were to be shipped in cryogenic conditions to the Advanced Photon Source for data collection. All diffraction data would be collected with a Rayonix MX300 at beamline 21-ID-F. Data would be collected sequentially with an incident wavelength of 0.97872 Å and Δϕ of 0.2° for all crystals, maintained at 100K. The data would be processed in HKL.[45, 46] Like with the solved "wild-type" SweetieTS and LiLac structures, they would be solved via chimeric molecular replacement, refined in Phenix,[49] and model building would be done in Coot.[48]

RESULTS II

K66H and L276V, SweetieTS mutants with a lower binding affinity, were crystallized in hopes of obtaining a SweetieTS structure that is unbound and resting in its low lifetime state. After quicker initial successes with K66H, in addition to its prospects as a GEFI with better coupling than L276V, crystallizing K66H took precedence over the L276V mutant. We prepared sparse matrix screens, began optimizing, and obtained birefringent, crystal-like entities, none of which have diffracted.

At the time of publication one crystal of LiLac F423A appreciably diffracted (2.10 Å). This LiLac mutant crystallized in 35% Tacsimate, pH 7, with lactate concentrations 10x that of the

protein. Samantha Horowitz is presently attempting to solve the structure via chimeric molecular replacement, which has proved more difficult than with the original LiLac.

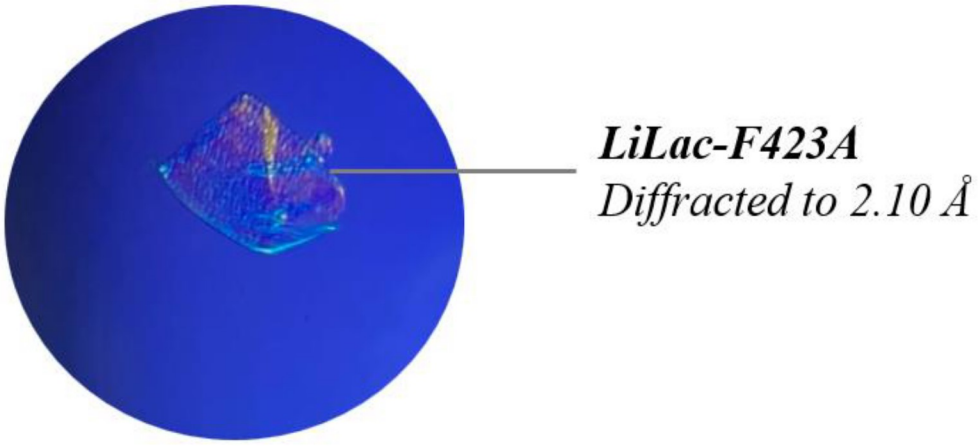

Figure 14. LiLac-F423A mutant. This crystal formed in a condition with only Tacsimate, a reagent developed for crystallography, comprised of organic salts.

ANALYSIS & DISCUSSION

At the time of publication, our work structurally characterizing the mechanisms of coupling and lifetime-change in the lactate-GEFI LiLac and the glucose-GEFI SweetieTS is ongoing. We have already obtained two crystal structures—an unbound LiLac and a bound SweetieTS. Though thorough characterization requires both bound and unbound states for each sensor, insights can be gained by comparing the mutagenesis reports from the Yellen Lab to the structures of the high-lifetime states of each sensor.

It is worth noting that both LiLac and SweetieTS structures are still pending validation, and as such, conclusions regarding side chain residues cannot be drawn unambiguously. However, as the real-space/reciprocal-space refinement process is complete, global conclusions about domain and backbone positioning can be drawn with confidence. For the purposes of this

discussion, I conducted Ramachandran, geometric, and rotamer analysis on the side chains of the key LiLac residues discussed in this section.

```
1   VSKGEELFTGVVPILVELDGDVNGHKFSVSGEGEGDATYGKLTLKFICTT
51  GKLPVPWPTLVTTLXVQCFARYPDHMKQHDFFKSAMPEGYVQERTIFFKD
101 DGNYKTRAEVKFEGDTLVNRIELKGIDFKEDGNILGHKLEYNSSGRTGID
151 PFTESVLQSQATELLQKKAQLVSFKIQGIMKRIFMGANTLEKFLSDENSA
201 INDTLKRRMLSEFLLANPHVLLVSAIYTNNNERVITAMSMDSKIAYPNTT
251 LNENMTNQIRSLKSITHSDPYYKEVNGDKIYGMDITLPLMGKNQNAIGAL
301 NFFLNIDAFYTDVVGKKKSNTFLMGKDGRLLINPNREIQDKILSAINPDR
351 RVAKAVEYYNQNEAGTLSYHSLSGNTETFLAIQPFDFFEEKGNNGNHWRW
401 AIGKYVNKSLVFSSHSNVYITADKQKNGIKANFKIRHNIEDGGVQLADHY
451 QQNTPIGDGPVLLPDNHYLSTQSKLSKDPNEKRDHMVLLEFVTAAGITLG
501 MDELY
```

Figure 15. LiLac sequence. Chromophore is listed as X (65). The fluorescent domain is listed in cyan, and the binding domain is listed in yellow. The N-terminal and C-terminal linkers are shown in green.

LiLac

The unpublished results of our collaborators' mutagenesis studies guided our process of structurally characterizing the coupling mechanisms in LiLac. Alanine point mutations, +1 insertions, or -1 deletions in the N terminal linker (S143 through T147) showed little effect on coupling or lifetime. Alanine point mutations were also made to the C-terminal linker (S413 through S416), which showed little change in lifetime or coupling. However, insertions and deletions here forced the low lifetime state. These mutagenesis studies suggest that (1) only one of the two linkers is actively involved in coupling, and (2) the length is more important than the identity of the side chains. Additionally, alanine mutations at F412, E472 and K474, which neighbor the linker, forced LiLac into a low-lifetime state. This suggests, (3) local residues are involved in the coupling process.

The crystal structure of LiLac in its high lifetime state offers exciting insights. Pertaining to the C terminal linker, the 4 residues that make up the linker assume a position in the seventh strand of the β barrel, fulfilling the position typically occupied by F146-N149 in mTurquoise. In the high-lifetime state shown, the β barrel is well sealed by the linker (**Figure 16**).

Moreover, F412, E472 and K474 residues are all in the local environment of the C-terminal linker, which is wedged between the adjacent β strands in the barrel (**Figure 17**). The side chain of F412 assumes a position *sandwiched* between E472 and K474.

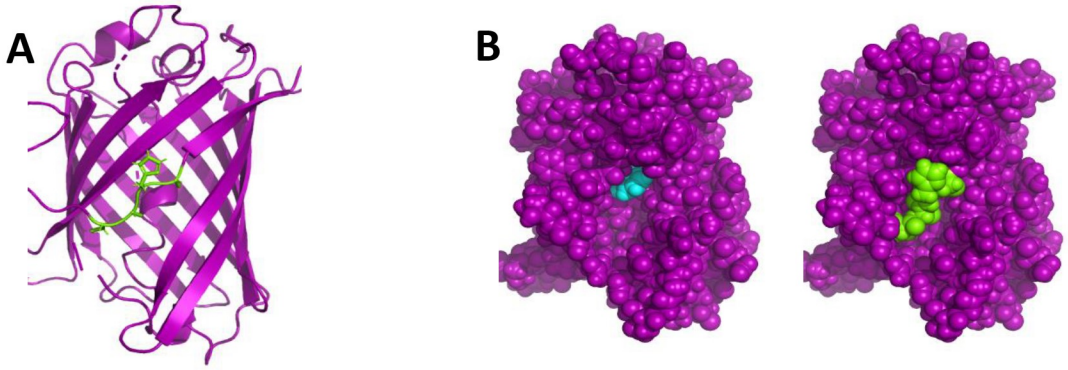

Figure 16. SSHS seals the barrel. **(A)** The C-terminal, S-S-H-S linker (chartreuse) fills the gap between two adjacent β strands. **(B)** Seen in this space filling model, the chromophore (cyan) is exposed when the linker is removed. The linker seals the barrel in the high-lifetime state. Generated in PyMOL.

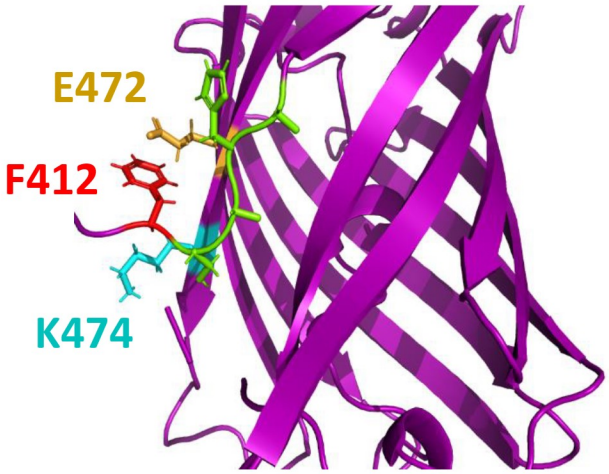

Figure 17. The linker's neighborhood. F412, E472, and K474 are in the local neighborhood of the linker. An alanine mutation at any of these residues kills coupling. Generated in PyMOL.

After overlaying LiLac with the published HpTlpC/lactate complex[39] (**Figure 8**), it became apparent that the Y369-T378 loop, shown in magenta in **Figure 18**, is displaced from the binding pocket in the absence of lactate. To bind lactate, the binding residues L372 and S373 would presumably fold back over the binding pocket, as shown in the published HpTlpC/lactate structure. This structural change would pull on the adjacent, antiparallel β strands, straining the C-terminal, S413-S416 linker.

A possible mechanism can be proposed. F412 forms a stabilizing interaction away from solvent between E472 and K474. This interaction is what our collaborator calls, the "latch." The latched phenylalanine, one residue upstream of the linker, renders the linker's proximate position in the barrel most stable. Upon lactate binding, the Y369-T378 loop would drastically change conformation, forcing adjacent, interacting β strands to move as well. This increased strain would overcome the phenylalanine latch and pull F412 and the linker out of their respective positions. In this hypothetical, bound-Lilac structure, the linker is free from the barrel, increasing solvent exchange inside the β barrel which would cause the lifetime to drop.

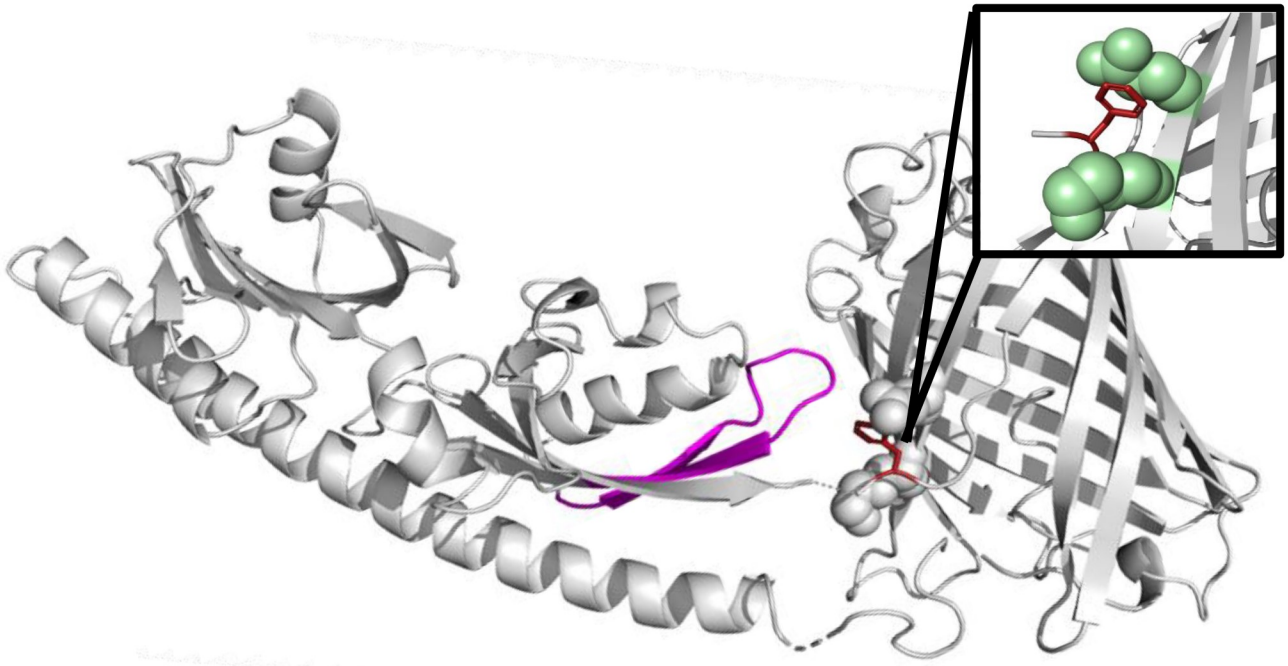

Figure 18. The LiLac "latch." F412 (maroon) interacting with neighboring residues E472 and K474 (mint green) and forming a stabilizing interaction that keeps the linker in the β barrel scaffold. Ligand binding, involving the drastic movement of the Y369-T378 loop (magenta), destabilizes the phenylalanine interaction keeping the linker in place. Generated in PyMOL.

This structure corroborates the hypotheses that (1) only one of the two linkers is actively involved in coupling, and (2) the length is more important than the identity of the side chains. An additional residue on the C-terminal linker would displace F412 from its latch position, removing this interaction that stabilizes the linker's position in the β barrel. Additional mutagenesis around the linker showed F423, E472 and K474 are pertinent residues, as alanine mutations here forced LiLac into a low-lifetime state. The crystal structure offers insights into *how* (3) local residues are involved in the coupling process: They participate in a "latch" mechanism.

```
1    SKLEIFSWWAGDEGPALEALIRLYKQKYPGVEVINATVTGGAGVNARAVL
51   KTRMLGGDPPDTFQVAAGMELIGTWVVANRMEDLSALFRQEGWLQAFPKG
101  LIDLISYKGGIWSVPVNIHRSNVMWYLPAKLKEWGVNPPRTWDEFLATCQ
151  TLKQKGLEAPLALGENWTQQHLWESVALAVLGPDDWNNLWNGKLKFTDPK
201  AVRAWEVFGRVLDCANKDAAGLSWQQAVDRVVQGKAAFNVMGDWAAGYMT
251  TTLKLKPGTDFAWAPSPGTQGVFMMLSDSFGLPKGAKNRQNAINWLRLVG
301  SKEGQDTFNPLKGSIAARLDSDPSKYPDSFTAHNVYIMADKQKNGIKANF
351  KIRHNIEDGGVQLADHYQQNTPIGDGPVLLPDNHYLSIQSKLSKDPNEKR
401  DHMVLLEFVTAAGITHGMDELYKGGTGGSMVSKGEELFTGVVPILVELDG
451  DVNGHKFSVSGEGEGDATYGKLTLKFICTTGKLPVPWPTLVTTFXVMVFA
501  RYPDHMKQHDFFKSAMPEGYVQERTIFFKDDGNYKTRAEVKFEGDTLVNR
551  IELKGIDFKEDGNILGHKLEYNEPNAYGQSAMRDWRSNRIVGSLVAGAVA
601  PESFMSQFGTVMEIFLQTRNPQAAANAAQAIADQVGLGRLG
```

Figure 19. SweetieTS sequence. Chromophore (495) is listed as X. The fluorescent domain is highlighted in cyan, and the binding domain is highlighted in yellow. The N-terminal and C-terminal linkers are shown in green. Additional SweetieTS residues are shown in grey.

SweetieTS

Our collaborators propose that a linker is also involved in sealing the β barrel in SweetieTS. Unlike the LiLac structure, the SweetieTS structure contains the seventh β strand in its standard position: The linker is not resting in the β barrel scaffold, and it does not prevent solvent from accessing the chromophore. Though the seventh strand is positioned in the barrel, its distance from the eighth β strand is larger than in a standard GFP. In avGFP, H148 and K166, on the seventh and eighth strand respectively, are 7.7 Å from one another. In SweetieTS, they are 8.5 Å (**Figure 20**). There are no crystal structures available of T-Sapphire—the FP in SweetieTS—to do a more direct comparison.

Our collaborators suggest that this widened gap in the barrel offers an alternative mechanism of lifetime change. If the unbound state of SweetieTS places a lateral strain on the seventh and eighth strands of the β barrel (blue and yellow in **Figure 20**), this "wishbone"-like movement could let solvent access the chromophore, causing its drop in lifetime. The solved SweetieTS structure is bound and existing in its high lifetime state, yet there is still a larger "hole in the barrel" than in a standard avGFP. Our collaborators suggest that the existence of this strain in SweetieTS's "high" lifetime state could explain Sweetie's baseline, low lifetimes.

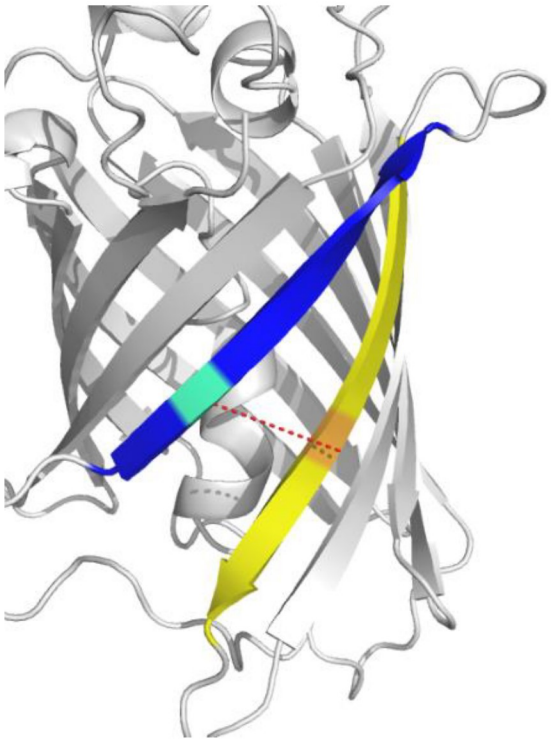

Figure 20. The SweetieTS "wishbone." The gap between H333 (cyan) and K351 (orange) in SweetieTS is 8.5 Å. Natively in avGFP, this gap is 7.7 Å, suggesting that there is pressure on the β barrel, even in the high lifetime state. Its important to note that its high lifetime of 1.95 ns is much lower than most GFPs. Generated in PyMOL.

This wishbone dynamic explains the mechanics that cause the GEFI's lifetime change: Lateral strain widens a gap, which lets solvent in to quench the chromophore. This model assumes an initial "lateral strain" on the seventh and eighth β barrel strands that is significantly stronger in the unbound state than the bound state. TtGBP belongs to a structural class of periplasmic binding proteins characterized by a hinge-like movement upon ligand binding. Two domains shift together to bind glucose and seal the binding pocket; they are shifted apart when unbound.[36] This suggests that the GBP could in fact cause more strain on the β barrel in the unbound formation than in the bound.

The mutagenesis studies offer additional insights to compare with the crystal structure. Any insertion, deletion or point mutation in SweetieTS's N terminal linker (P327 through A332) kills coupling and forces the low lifetime state. These residues are involved in coupling.

In the crystal SweetieTS structure, D328 on the N-terminal linker is 4.2 Å away from K391 on the side of the β barrel. Though too far to indicate the presence of a hydrogen bond or salt bridge, slight rotational fluctuations would bring the residues within the appropriate distance. Moreover, an alanine mutation at the K391 position also kills coupling, suggesting there is some interaction involving the lysine. Our collaborators propose that a salt bridge at this location could serve as a stabilizing interaction. When bound, and the GBP is closed, the salt-bridge provides additional stabilization in favor of the closed—or rather, relaxed—wishbone.

Due to challenges manipulating the restraints file for the SYG chromophore, these side chains have not been validated, so the confidence in claims regarding their side chain interactions is lower than in a finalized structure. Once validated, the 4.2 Å interaction between K391 and D328 could very well be within the 3.2 Å range of a salt bridge. Interestingly, a K391H mutation

improves coupling, and raises the maximal lifetime from 1.95 ns in SweetieTS to 2.6 ns. This K391H mutation has been referred to as the "K66H" mutation previously, a reference to a designation made while ordering the plasmid. An alternative theory is that a weaker interaction between D328 and K391 provides possible room for a histidine mutation to drastically improve coupling by forming a stronger salt bridge. These questions are important to discuss; however, without a fully validated structure, they are not quite ready to answer.

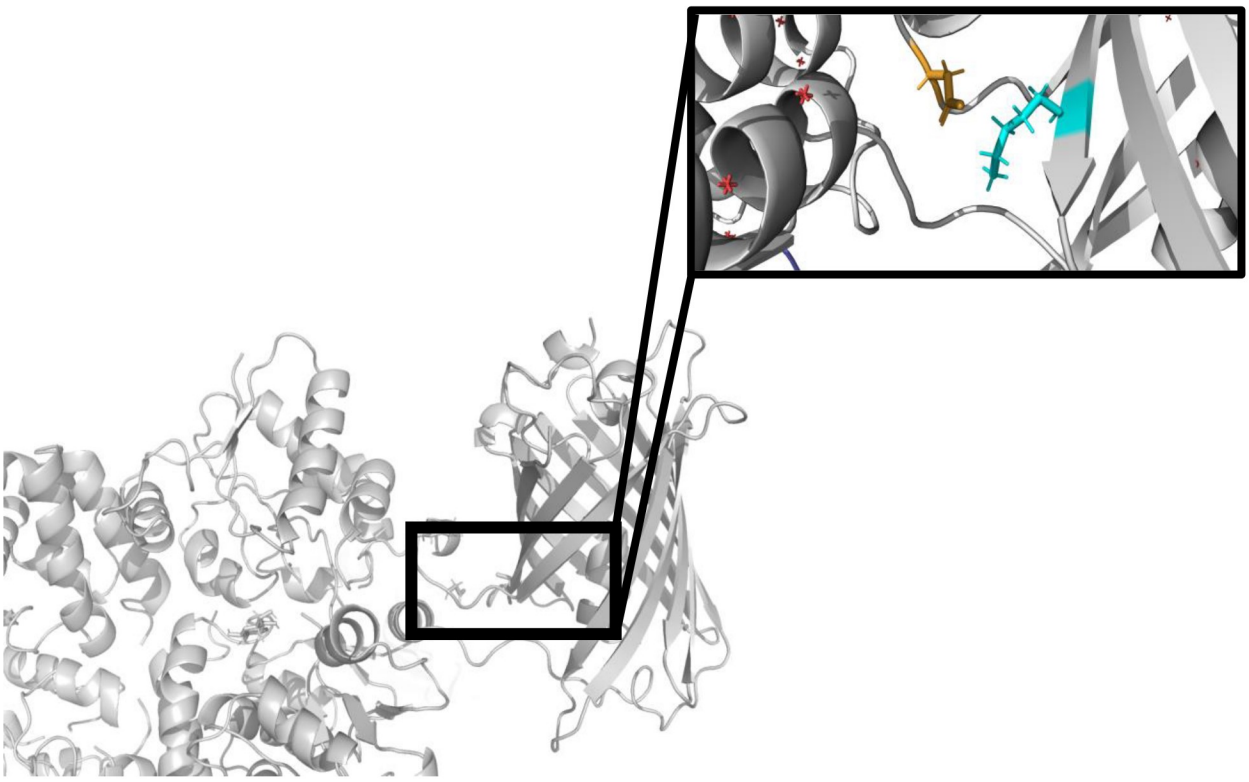

Figure 21. The SweetieTS salt bridge. K391 (cyan) and D328 (orange) are 4.2 Å apart. Although, there is no other obvious stabilizing interaction that K391 could be engaging in that would reflect its importance to coupling. Generated in PyMOL.

Similarly to LiLac, one linker is likely involved in coupling. Though, unlike with the LiLac structure, the linker's length and side chain identity is vital to coupling and lifetime change. Drawing on structural information, the side chains of other residues in the linker could be crucial in positioning the D328 where needed to engage with a cation on the GFP domain. In this case, linker length is also important, as an additional residue could push the aspartate out of range of the cationic lysine. An alanine mutation at this K391 residue kills coupling, suggesting that the side chain plays a determining role in the coupling process, as supported by the crystal structure.

CONCLUSION

Drawing unambiguous conclusions about the mechanisms of lifetime change in these GEFIs requires structures of bound LiLac and unbound SweetieTS. Immediate steps forward consist of solving the LiLac-F423A structure, and if bound, comparing the structure with our unbound LiLac structure. For SweetieTS, more K66H and L276V should be expressed so that crystallization conditions can continue to be optimized. Then, their structures can be solved, and if unbound, they can be compared with the bound SweetieTS structure.

Until then, we have tentative conclusions, subject to change with both the validation process and the solution of additional structures. To summarize, on each sensor one linker plays a key role in regulating the amount of solvent that has access to the chromophore. In LiLac, the linker's role is more direct: Its placement seals the "hole" in the β barrel, supported by a phenylalanine "latch" motif on residues near the linker. This emphasizes the importance of the local residues surrounding the linker with regards to coupling.

The linker in SweetieTS pulls on the seventh β strand, laterally opening the barrel like a "wishbone." This process also permits the same solvent exchange into the β barrel, which would quench fluorescence. Without validation it is difficult to confirm or deny, but an aspartate residue and lysine residue near the linker might engage in a salt bridge interaction that stabilizes the high-lifetime state. This would explain why mutations in either of these positions force the low lifetime state. These insights, especially when complimented by the additional crystal structures we are hoping to solve, could reveal potential ways of modifying these sensors and improve coupling.

Moreover, these structural studies not only provide general information about lifetime sensor coupling that could guide the design of novel biosensors, but they also provide examples of distinct motifs that enhance coupling. These motifs could perhaps be applied directly in the design of other biosensors. LiLac, SweetieTS, and other lifetime biosensors can provide quantitative metabolite concentrations *in vivo* and *ex vivo* and could aid in the development of novel treatments for neurological disease. An additional merit of this work is that these sensors are not limited to the scope of energy metabolism, nor brain tissue specifically. Fluorescence lifetime technology could be utilized to study a number of metabolic processes throughout the human body and advance the development of novel treatments.

REFERENCES

(1) Lu, S.; Huang, W.; Wang, Q.; Shen, Q.; Li, S.; Nussinov, R.; Zhang, J. The structural basis of ATP as an allosteric modulator. *PLoS Comput Biol* **2014**, *10* (9), e1003831. DOI: 10.1371/journal.pcbi.1003831 From NLM Medline.

(2) Yu, L.; Jin, J.; Xu, Y.; Zhu, X. Aberrant Energy Metabolism in Alzheimer's Disease. *J Transl Int Med* **2022**, *10* (3), 197-206. DOI: 10.2478/jtim-2022-0024 From NLM PubMed-not-MEDLINE.

(3) Lutas, A.; Yellen, G. The ketogenic diet: metabolic influences on brain excitability and epilepsy. *Trends Neurosci* **2013**, *36* (1), 32-40. DOI: 10.1016/j.tins.2012.11.005 From NLM Medline.

(4) Han, R.; Liang, J.; Zhou, B. Glucose Metabolic Dysfunction in Neurodegenerative Diseases-New Mechanistic Insights and the Potential of Hypoxia as a Prospective Therapy Targeting Metabolic Reprogramming. *Int J Mol Sci* **2021**, *22* (11). DOI: 10.3390/ijms22115887 From NLM Medline.

(5) Stafstrom, C. E.; Carmant, L. Seizures and epilepsy: an overview for neuroscientists. *Cold Spring Harb Perspect Med* **2015**, *5* (6). DOI: 10.1101/cshperspect.a022426 From NLM Medline.

(6) Tanner, G. R.; Lutas, A.; Martinez-Francois, J. R.; Yellen, G. Single K ATP channel opening in response to action potential firing in mouse dentate granule neurons. *J Neurosci* **2011**, *31* (23), 8689-8696. DOI: 10.1523/JNEUROSCI.5951-10.2011 From NLM Medline.

(7) Ashcroft, F. M.; Gribble, F. M. Correlating structure and function in ATP-sensitive K+ channels. *Trends Neurosci* **1998**, *21* (7), 288-294. DOI: 10.1016/s0166-2236(98)01225-9 From NLM Medline.

(8) Lian, X. Y.; Khan, F. A.; Stringer, J. L. Fructose-1,6-bisphosphate has anticonvulsant activity in models of acute seizures in adult rats. *J Neurosci* **2007**, *27* (44), 12007-12011. DOI: 10.1523/JNEUROSCI.3163-07.2007 From NLM Medline.

(9) Juge, N.; Gray, J. A.; Omote, H.; Miyaji, T.; Inoue, T.; Hara, C.; Uneyama, H.; Edwards, R. H.; Nicoll, R. A.; Moriyama, Y. Metabolic control of vesicular glutamate transport and release. *Neuron* **2010**, *68* (1), 99-112. DOI: 10.1016/j.neuron.2010.09.002 From NLM Medline.

(10) Díaz-García, C. M.; Lahmann, C.; Martínez-François, J. R.; Li, B.; Koveal, D.; Nathwani, N.; Rahman, M.; Keller, J. P.; Marvin, J. S.; Looger, L. L.; et al. Quantitative in vivo imaging of neuronal glucose concentrations with a genetically encoded fluorescence lifetime sensor. *Journal of Neuroscience Research* **2019**, *97* (8), 946-960. DOI: https://doi.org/10.1002/jnr.24433.

(11) Sibson, N. R.; Dhankhar, A.; Mason, G. F.; Rothman, D. L.; Behar, K. L.; Shulman, R. G. Stoichiometric coupling of brain glucose metabolism and glutamatergic neuronal activity. *Proc Natl Acad Sci U S A* **1998**, *95* (1), 316-321. DOI: 10.1073/pnas.95.1.316 From NLM Medline.

(12) Parsons-Davis, T.; Knight, K.; Fitzgerald, M.; Stone, G.; Caldeira, L.; Ramon, C.; Kristo, M. Application of modern autoradiography to nuclear forensic analysis. *Forensic Sci Int* **2018**, *286*, 223-232. DOI: 10.1016/j.forsciint.2018.03.027 From NLM PubMed-not-MEDLINE.

(13) Moses, W. W. Fundamental Limits of Spatial Resolution in PET. *Nucl Instrum Methods Phys Res A* **2011**, *648 Supplement 1*, S236-S240. DOI: 10.1016/j.nima.2010.11.092 From NLM PubMed-not-MEDLINE.

(14) M. Carter, R. E., N. Golstein, and M. Iyer. Microscopy. In *Guide to Research Techniques in Neuroscience*, 3 ed.; Academic Press, 2022; pp 115-143.

(15) Yellen, G.; Mongeon, R. Quantitative two-photon imaging of fluorescent biosensors. *Curr Opin Chem Biol* **2015**, *27*, 24-30. DOI: 10.1016/j.cbpa.2015.05.024 From NLM Medline.

(16) Koveal, D.; Diaz-Garcia, C. M.; Yellen, G. Fluorescent Biosensors for Neuronal Metabolism and the Challenges of Quantitation. *Curr Opin Neurobiol* **2020**, *63*, 111-121. DOI: 10.1016/j.conb.2020.02.011 From NLM Medline.

(17) Diem, A. K.; Tan, M.; Bressloff, N. W.; Hawkes, C.; Morris, A. W.; Weller, R. O.; Carare, R. O. A Simulation Model of Periarterial Clearance of Amyloid-beta from the Brain. *Front Aging Neurosci* **2016**, *8*, 18. DOI: 10.3389/fnagi.2016.00018 From NLM PubMed-not-MEDLINE.

(18) Shami, G. J.; Cheng, D.; Verhaegh, P.; Koek, G.; Wisse, E.; Braet, F. Three-dimensional ultrastructure of giant mitochondria in human non-alcoholic fatty liver disease. *Sci Rep* **2021**, *11* (1), 3319. DOI: 10.1038/s41598-021-82884-z From NLM Medline.

(19) Feher, J. Cell Structure. In *Quantitative Human Physiology*, 2 ed.; Feher, J. Ed.; Academic Press, 2017; pp 101-119.

(20) Brown, A.; Baird, M. R.; Yip, M. C.; Murray, J.; Shao, S. Structures of translationally inactive mammalian ribosomes. *Elife* **2018**, *7*. DOI: 10.7554/eLife.40486 From NLM Medline.

(21) Choi, M.; Kwok, S. J.; Yun, S. H. In vivo fluorescence microscopy: lessons from observing cell behavior in their native environment. *Physiology (Bethesda)* **2015**, *30* (1), 40-49. DOI: 10.1152/physiol.00019.2014 From NLM Medline.

(22) Tantama, M.; Hung, Y. P.; Yellen, G. Optogenetic reporters: Fluorescent protein-based genetically encoded indicators of signaling and metabolism in the brain. *Prog Brain Res* **2012**, *196*, 235-263. DOI: 10.1016/B978-0-444-59426-6.00012-4 From NLM Medline.

(23) Pittet, M. J.; Weissleder, R. Intravital imaging. *Cell* **2011**, *147* (5), 983-991. DOI: 10.1016/j.cell.2011.11.004 From NLM Medline.

(24) Miyawaki, A.; Llopis, J.; Heim, R.; McCaffery, J. M.; Adams, J. A.; Ikura, M.; Tsien, R. Y. Fluorescent indicators for Ca2+ based on green fluorescent proteins and calmodulin. *Nature* **1997**, *388* (6645), 882-887. DOI: 10.1038/42264 From NLM Medline.

(25) Keller, J. P.; Marvin, J. S.; Lacin, H.; Lemon, W. C.; Shea, J.; Kim, S.; Lee, R. T.; Koyama, M.; Keller, P. J.; Looger, L. L. In vivo glucose imaging in multiple model organisms with an engineered single-wavelength sensor. *Cell Rep* **2021**, *35* (12), 109284. DOI: 10.1016/j.celrep.2021.109284 From NLM Medline.

(26) Okumoto, S.; Takanaga, H.; Frommer, W. B. Quantitative imaging for discovery and assembly of the metabo-regulome. *New Phytol* **2008**, *180* (2), 271-295. DOI: 10.1111/j.1469-8137.2008.02611.x From NLM Medline.

(27) Chudakov, D. M.; Matz, M. V.; Lukyanov, S.; Lukyanov, K. A. Fluorescent proteins and their applications in imaging living cells and tissues. *Physiol Rev* **2010**, *90* (3), 1103-1163. DOI: 10.1152/physrev.00038.2009 From NLM Medline.

(28) Day, R. N.; Davidson, M. W. The fluorescent protein palette: tools for cellular imaging. *Chem Soc Rev* **2009**, *38* (10), 2887-2921. DOI: 10.1039/b901966a From NLM Medline.

(29) Remington, S. J. Green fluorescent protein: a perspective. *Protein Sci* **2011**, *20* (9), 1509-1519. DOI: 10.1002/pro.684 From NLM Medline.

(30) Remington, S. J. Fluorescent proteins: maturation, photochemistry and photophysics. *Curr Opin Struct Biol* **2006**, *16* (6), 714-721. DOI: 10.1016/j.sbi.2006.10.001 From NLM Medline.

(31) Berezin, M. Y.; Achilefu, S. Fluorescence lifetime measurements and biological imaging. *Chem Rev* **2010**, *110* (5), 2641-2684. DOI: 10.1021/cr900343z From NLM Medline.

(32) Ormo, M.; Cubitt, A. B.; Kallio, K.; Gross, L. A.; Tsien, R. Y.; Remington, S. J. Crystal structure of the Aequorea victoria green fluorescent protein. *Science* **1996**, *273* (5280), 1392-1395. DOI: 10.1126/science.273.5280.1392 From NLM Medline.

(33) Wallace, A. C.; Laskowski, R. A.; Thornton, J. M. LIGPLOT: a program to generate schematic diagrams of protein-ligand interactions. *Protein Eng* **1995**, *8* (2), 127-134. DOI: 10.1093/protein/8.2.127 From NLM Medline.

(34) Trigo-Mourino, P.; Thestrup, T.; Griesbeck, O.; Griesinger, C.; Becker, S. Dynamic tuning of FRET in a green fluorescent protein biosensor. *Sci Adv* **2019**, *5* (8), eaaw4988. DOI: 10.1126/sciadv.aaw4988 From NLM Medline.

(35) Koveal, D.; Rosen, P. C.; Meyer, D. J.; Diaz-Garcia, C. M.; Wang, Y.; Cai, L. H.; Chou, P. J.; Weitz, D. A.; Yellen, G. A high-throughput multiparameter screen for accelerated development and optimization of soluble genetically encoded fluorescent biosensors. *Nat Commun* **2022**, *13* (1), 2919. DOI: 10.1038/s41467-022-30685-x From NLM Medline.

(36) Cuneo, M. J.; Changela, A.; Warren, J. J.; Beese, L. S.; Hellinga, H. W. The crystal structure of a thermophilic glucose binding protein reveals adaptations that interconvert mono and di-saccharide binding sites. *J Mol Biol* **2006**, *362* (2), 259-270. DOI: 10.1016/j.jmb.2006.06.084 From NLM Medline.

(37) Zapata-Hommer, O.; Griesbeck, O. Efficiently folding and circularly permuted variants of the Sapphire mutant of GFP. *BMC Biotechnol* **2003**, *3*, 5. DOI: 10.1186/1472-6750-3-5 From NLM Medline.

(38) Diaz-Garcia, C. M.; Mongeon, R.; Lahmann, C.; Koveal, D.; Zucker, H.; Yellen, G. Neuronal Stimulation Triggers Neuronal Glycolysis and Not Lactate Uptake. *Cell Metab* **2017**, *26* (2), 361-374 e364. DOI: 10.1016/j.cmet.2017.06.021 From NLM Medline.

(39) Machuca, M. A.; Johnson, K. S.; Liu, Y. C.; Steer, D. L.; Ottemann, K. M.; Roujeinikova, A. Helicobacter pylori chemoreceptor TlpC mediates chemotaxis to lactate. *Sci Rep* **2017**, *7* (1), 14089. DOI: 10.1038/s41598-017-14372-2 From NLM Medline.

(40) Goedhart, J.; van Weeren, L.; Hink, M. A.; Vischer, N. O.; Jalink, K.; Gadella, T. W., Jr. Bright cyan fluorescent protein variants identified by fluorescence lifetime screening. *Nat Methods* **2010**, *7* (2), 137-139. DOI: 10.1038/nmeth.1415 From NLM Medline.

(41) Shinobu, A.; Agmon, N. The hole in the barrel: water exchange at the GFP chromophore. *J Phys Chem B* **2015**, *119* (8), 3464-3478. DOI: 10.1021/jp5127255 From NLM Medline.

(42) Dessau, M. A.; Modis, Y. Protein crystallization for X-ray crystallography. *J Vis Exp* **2011**, (47). DOI: 10.3791/2285 From NLM Medline.

(43) Watson, A. A.; O'Callaghan, C. A. Crystallization and X-ray diffraction analysis of human CLEC-2. *Acta Crystallogr Sect F Struct Biol Cryst Commun* **2005**, *61* (Pt 12), 1094-1096. DOI: 10.1107/S1744309105037991 From NLM Medline.

(44) Wienen-Schmidt, B.; Oebbeke, M.; Ngo, K.; Heine, A.; Klebe, G. Two Methods, One Goal: Structural Differences between Cocrystallization and Crystal Soaking to Discover Ligand Binding Poses. *ChemMedChem* **2021**, *16* (1), 292-300. DOI: 10.1002/cmdc.202000565 From NLM Medline.

(45) Kabsch, W. Xds. *Acta Crystallogr D Biol Crystallogr* **2010**, *66* (Pt 2), 125-132. DOI: 10.1107/S0907444909047337 From NLM Medline.

(46) Evans, P. R.; Murshudov, G. N. How good are my data and what is the resolution? *Acta Crystallogr D Biol Crystallogr* **2013**, *69* (Pt 7), 1204-1214. DOI: 10.1107/S0907444913000061 From NLM Medline.

(47) McCoy, A. J.; Grosse-Kunstleve, R. W.; Adams, P. D.; Winn, M. D.; Storoni, L. C.; Read, R. J. Phaser crystallographic software. *J Appl Crystallogr* **2007**, *40* (Pt 4), 658-674. DOI: 10.1107/S0021889807021206 From NLM PubMed-not-MEDLINE.

(48) Emsley, P.; Lohkamp, B.; Scott, W. G.; Cowtan, K. Features and development of Coot. *Acta Crystallogr D Biol Crystallogr* **2010**, *66* (Pt 4), 486-501. DOI: 10.1107/S0907444910007493 From NLM Medline.

(49) Adams, P. D.; Afonine, P. V.; Bunkoczi, G.; Chen, V. B.; Davis, I. W.; Echols, N.; Headd, J. J.; Hung, L. W.; Kapral, G. J.; Grosse-Kunstleve, R. W.; et al. PHENIX: a comprehensive Python-based system for macromolecular structure solution. *Acta Crystallogr D Biol Crystallogr* **2010**, *66* (Pt 2), 213-221. DOI: 10.1107/S0907444909052925 From NLM Medline.

(50) Barondeau, D. P.; Kassmann, C. J.; Tainer, J. A.; Getzoff, E. D. Understanding GFP posttranslational chemistry: structures of designed variants that achieve backbone fragmentation, hydrolysis, and decarboxylation. *J Am Chem Soc* **2006**, *128* (14), 4685-4693. DOI: 10.1021/ja056635l From NLM Medline.

(51) Oldfield, C. J.; Xue, B.; Van, Y. Y.; Ulrich, E. L.; Markley, J. L.; Dunker, A. K.; Uversky, V. N. Utilization of protein intrinsic disorder knowledge in structural proteomics. *Biochim Biophys Acta* **2013**, *1834* (2), 487-498. DOI: 10.1016/j.bbapap.2012.12.003 From NLM Medline.